Article

The CYGNO Experiment

Fernando Domingues Amaro [1], Elisabetta Baracchini [2,3], Luigi Benussi [4], Stefano Bianco [4], Cesidio Capoccia [4], Michele Caponero [4,5], Danilo Santos Cardoso [6], Gianluca Cavoto [7,8], André Cortez [2,3], Igor Abritta Costa [9], Rita Joanna da Cruz Roque [1], Emiliano Dané [4], Giorgio Dho [2,3], Flaminia Di Giambattista [2,3], Emanuele Di Marco [7], Giovanni Grilli di Cortona [4], Giulia D'Imperio [7], Francesco Iacoangeli [7], Herman Pessoa Lima Júnior [6], Guilherme Sebastiao Pinheiro Lopes [9], Amaro da Silva Lopes Júnior [9], Giovanni Maccarrone [4], Rui Daniel Passos Mano [1], Michela Marafini [10], Robert Renz Marcelo Gregorio [11], David José Gaspar Marques [2,3], Giovanni Mazzitelli [4], Alasdair Gregor McLean [11], Andrea Messina [7,8], Cristina Maria Bernardes Monteiro [1], Rafael Antunes Nobrega [9], Igor Fonseca Pains [9], Emiliano Paoletti [4], Luciano Passamonti [4], Sandro Pelosi [7], Fabrizio Petrucci [12,13], Stefano Piacentini [7,8], Davide Piccolo [4], Daniele Pierluigi [4], Davide Pinci [7,*], Atul Prajapati [2,3], Francesco Renga [7], Filippo Rosatelli [4], Alessandro Russo [4], Joaquim Marques Ferreira dos Santos [1], Giovanna Saviano [4,14], Neil John Curwen Spooner [11], Roberto Tesauro [4], Sandro Tomassini [4] and Samuele Torelli [2,3]

1   LIBPhys, Department of Physics, University of Coimbra, 3004-516 Coimbra, Portugal; famaro@uc.pt (F.D.A.); ritaroque@fis.uc.pt (R.J.d.C.R.); RDPMano@uc.pt (R.D.P.M.); cristinam@uc.pt (C.M.B.M.); jmf@uc.pt (J.M.F.d.S.)
2   Gran Sasso Science Institute, 67100 L'Aquila, Italy; elisabetta.baracchini@gssi.it (E.B.); andre.f.cortez@gmail.com (A.C.); giorgio.dho@gssi.it (G.D.); flaminia.digiambattista@gssi.it (F.D.G.); david.marques@gssi.it (D.J.G.M.); atul.prajapati@gssi.it (A.P.); samuele.torelli@gssi.it (S.T.)
3   Istituto Nazionale di Fisica Nucleare, Laboratori Nazionali del Gran Sasso, 67100 Assergi, Italy
4   Istituto Nazionale di Fisica Nucleare, Laboratori Nazionali di Frascati, 00044 Frascati, Italy; luigi.benussi@lnf.infn.it (L.B.); stefano.bianco@lnf.infn.it (S.B.); Cesidio.Capoccia@lnf.infn.it (C.C.); michele.caponero@enea.it (M.C.); Emiliano.Dane@lnf.infn.it (E.D.); grillidc@lnf.infn.it (G.G.d.C.); giovanni.maccarrone@lnf.infn.it (G.M.); giovanni.mazzitelli@lnf.infn.it (G.M.); Emiliano.Paoletti@lnf.infn.it (E.P.); luciano.passamonti@lnf.infn.it (L.P.); Davide.Piccolo@lnf.infn.it (D.P.); Daniele.Pierluigi@lnf.infn.it (D.P.); filippo.rosatelli@lnf.infn.it (F.R.); arusso@lnf.infn.it (A.R.); giovanna.saviano@cern.ch (G.S.); Roberto.Tesauro@lnf.infn.it (R.T.); sandro.tomassini@lnf.infn.it (S.T.)
5   ENEA Centro Ricerche Frascati, 00044 Frascati, Italy
6   Centro Brasileiro de Pesquisas Físicas, Rio de Janeiro 22290-180, RJ, Brazil; dsantoscardoso@outlook.com (D.S.C.); hlima@cbpf.br (H.P.L.J.)
7   Istituto Nazionale di Fisica Nucleare, Sezione di Roma, 00185 Roma, Italy; gianluca.cavoto@roma1.infn.it (G.C.); emanuele.dimarco@roma1.infn.it (E.D.M.); giulia.dimperio@roma1.infn.it (G.D.); francesco.iacoangeli@roma1.infn.it (F.I.); andrea.messina@uniroma1.it (A.M.); Alessandro.Pelosi@roma1.infn.it (S.P.); stefano.piacentini@uniroma1.it (S.P.); francesco.renga@roma1.infn.it (F.R.)
8   Dipartimento di Fisica, Sapienza Università di Roma, 00185 Roma, Italy
9   Faculdade de Engenharia, Universidade Federal de Juiz de Fora, Juiz de Fora 36036-900, MG, Brazil; igorabritta@gmail.com (I.A.C.); guilherme.lopes@engenharia.ufjf.br (G.S.P.L.); amaro.lopes@engenharia.ufjf.br (A.d.S.L.J.); rafael.nobrega@ufjf.edu.br (R.A.N.); igor.pains@engenharia.ufjf.br (I.F.P.)
10 Museo Storico della Fisica e Centro Studi e Ricerche "Enrico Fermi", Piazza del Viminale 1, 00184 Roma, Italy; Michela.Marafini@roma1.infn.it
11 Department of Physics and Astronomy, University of Sheffield, Sheffield S3 7RH, UK; robert.gregorio@sheffield.ac.uk (R.R.M.G.); ali.mclean@sheffield.ac.uk (A.G.M.); n.spooner@sheffield.ac.uk (N.J.C.S.)
12 Dipartimento di Matematica e Fisica, Università Roma TRE, 00146 Roma, Italy; fabrizio.petrucci@uniroma3.it
13 Istituto Nazionale di Fisica Nucleare, Sezione di Roma TRE, 00146 Roma, Italy
14 Dipartimento di Ingegneria Chimica, Materiali e Ambiente, Sapienza Università di Roma, 00185 Roma, Italy
*   Correspondence: davide.pinci@roma1.infn.it

Abstract: The search for a novel technology able to detect and reconstruct nuclear and electron recoil events with the energy of a few keV has become more and more important now that large regions of high-mass dark matter (DM) candidates have been excluded. Moreover, a detector sensitive to incoming particle direction will be crucial in the case of DM discovery to open the possibility

of studying its properties. Gaseous time projection chambers (TPC) with optical readout are very promising detectors combining the detailed event information provided by the TPC technique with the high sensitivity and granularity of latest-generation scientific light sensors. The CYGNO experiment (a CYGNus module with Optical readout) aims to exploit the optical readout approach of multiple-GEM structures in large volume TPCs for the study of rare events as interactions of low-mass DM or solar neutrinos. The combined use of high-granularity sCMOS cameras and fast light sensors allows the reconstruction of the 3D direction of the tracks, offering good energy resolution and very high sensitivity in the few keV energy range, together with a very good particle identification useful for distinguishing nuclear recoils from electronic recoils. This experiment is part of the CYGNUS proto-collaboration, which aims at constructing a network of underground observatories for directional DM search. A one cubic meter demonstrator is expected to be built in 2022/23 aiming at a larger scale apparatus (30 m^3–100 m^3) at a later stage.

1. Introduction

The presence in the universe of large amounts of non-luminous matter (usually referred to as dark matter (DM)) is nowadays an established, yet still mysterious, paradigm [1]. Deciphering its essence is one of the most compelling tasks for fundamental physics today. Electrically neutral and very low interacting particles with a mass in the range of few to thousands of GeV are usually referred to as *weakly interacting massive particles (WIMPs)*, and represent a well-motivated DM candidate independently predicted by the extension of the Standard Model of particle physics and the Λ-CDM model of cosmology. The measurements of the rotational curve of our galaxy suggests the presence of a DM halo, through which ordinary, luminous galactic matter is travelling in its rotation around the galactic center. This creates a relative motion between an observer on Earth and the particles in the halo that scientists seek to exploit to detect DM through their elastic scattering with ordinary matter. In particular, low-energy (1–100 keV) nuclear recoils (NR) are expected to be the clearest evidence of WIMP interactions.

Given their rarity, the main experimental challenge of direct DM searches in the GeV mass region is to discriminate NR from interactions induced by other particles, which have largely higher rates. The apparent WIMP wind would create two peculiar effects for an observer on Earth, which can be exploited for a positive identification of a DM signal. Since, in its rotation around the Sun, the Earth's orbital velocity is anti-parallel to the DM wind during summer and parallel during winter, the observed DM rates inside the detector are expected to display a seasonal modulation of a few percent. A much more robust signature is provided by the diurnal directional modulation of the DM signal. The peak flux, in fact, is expected to come from the direction of solar motion around the center of our galaxy, which happens to point towards the Cygnus constellation. Due to the Earth's rotation around its axis (oriented at 48° with respect to the direction of the apparent DM wind), an observer on Earth would see the average incoming direction of DM changing by ∼96° every 12 sidereal hours. The amplitude of the direction modulation depends on the relative angle between the laboratory frame and the Earth axis, with the maximum at 45° inclination and no modulation along directions parallel to the axis.

The determination of the incoming direction of the WIMP can therefore provide useful information to infer a correlation with an astrophysical source [2] that no source of background can mimic. Directional measurements can furthermore discriminate between various DM halo models and provide constraints on WIMP properties, unlike conventional non-directional detectors [2].

While the last few decades have seen enormous advances in direct DM searches, leading to many orders of magnitude of improvement for masses larger than 10 GeV, the O(GeV) mass range still remains theoretically well-motivated [3–5]. Despite the great

effort devoted to lowering the threshold for nuclear recoils to include DM scattering directly from electrons [6–11] or to exploit new signatures such as the Migdal effect [12–16] and photon bremsstrahlung [17], the O(GeV) mass range is still largely unexplored.

Given the kinematics of elastic scattering, a direct DM detection experiment achieves its best sensitivity for WIMP masses equal to the target mass nuclei. The maximum fraction ϵ of the energy that can be transferred to a target of mass m_T by a WIMP of mass m_χ is in fact given by:

$$\epsilon = \frac{4\rho}{(\rho + 1)^2} \tag{1}$$

with $\rho = \frac{m_T}{m_\chi}$. Therefore, low-mass target nuclei, such as hydrogen and helium, are the best choices to maximise the sensitivity to O(GeV) WIMP masses.

The CYGNO experiment proposes an innovative approach to the direct DM search challenge. A high-resolution 3D gaseous time projection chamber (TPC) operated at atmospheric pressure is employed with low-mass target nuclei, such as helium and fluorine, to boost the sensitivity to O(GeV) WIMP masses for both spin- independent (SI) and spin-dependent (SD) couplings. It is also important to notice that low mass nuclei will result in longer track lengths, easing the determination of their direction and thus increasing directional sensitivity. Studies to add a hydrogen-based gas to provide even lighter targets are ongoing. The topological signature of the recoil event also improves particle identification and hence rejection of natural radioactivity backgrounds, in particular electron recoils (ER) produced by photon interactions down to low energy thresholds. The possibility of operation at atmospheric pressure guarantees a reasonable volume-to-target-mass ratio, while at the same time allowing for a reduction in the engineering requirements of the vessel (hence internal backgrounds). The possibility of a high resolution 3D TPC, such as the one foreseen by this project, will allow CYGNO to explore new physics cases including, among others, the elastic scattering of sub-GeV DM [18] and of solar neutrinos [19,20]. Moreover, operating at atmospheric pressure would allow a high-mass target to be exposed without the need of very large volumes.

The results obtained with current prototypes (Section 3) are the basis for the design of a 1 m³ demonstrator that is the subject of this paper. According to the performance of this, the collaboration will propose a larger detector for a competitive experiment. With this program, CYGNO fits in the context of the wider international CYGNUS effort to establish a galactic directional recoil observatory that can test the DM hypothesis beyond the neutrino floor and measure the coherent scattering of neutrinos from the Sun and supernovae [21].

2. The Experimental Approach

The CYGNO experiment goal is to deploy at INFN Gran Sasso Laboratories (LNGS) a high-resolution TPC with optical readout based on gas electron multipliers (GEMs) working with a helium/fluorine-based gas mixture at atmospheric pressure for the study of rare events with energy releases in the range between hundreds of eV up to tens of keV.

Although challenging, gaseous TPCs constitute a promising approach to directional DM searches providing a set of crucial features:

- TPCs usually comprise a sensitive volume, filled with gas or liquid, enclosed between an anode and a cathode generating a suitable electric field in it [22–24]. The passage of an ionising particle produces free electrons and ions that start to drift towards the above-mentioned electrodes. These are usually segmented and read out to provide granular information about the charge collection point on the plane. The third coordinate can be evaluated from the drift time measurement. Therefore, TPCs are inherently 3D detectors capable of acquiring large sensitive volumes with a lower amount of readout channels with respect to other high-precision 3D tracking systems;
- Gaseous detectors can feature very low-energy detection thresholds. A single electron cluster can be produced with energy releases of the order of few tens of eV and,

in gases, this has a very good chance of reaching the multiplication region to produce a detectable signal;

- A measurement of the total ionisation indicates the energy released by the recoil, and (depending on the readout plane granularity) the profile of the energy deposit along the track can be measured with high precision, providing excellent background discrimination;
- Depending on the energy and mass of the recoiling particle and on the gas density, the track itself indicates the axis of the recoil, and the charge profile along it encodes the track orientation (*head-tail*), providing an additional powerful observable for DM searches;
- A large choice of gasses can be employed in TPCs, including light nuclei with an odd number of nucleons (such as fluorine), which are also sensitive to both SI and SD interactions in the O(GeV) mass region;
- A room-temperature and atmospheric-pressure detector results in operational and economical advantages, with no need for cooling or vacuum sealing. These choices allow for a simpler technology and experiment realization and more straightforward scaling when compared to cryogenic solutions currently dominating the DM direct search scene;
- The use of a gaseous target reduces the interaction probability with respect to denser material (liquid or solid). Nevertheless, TPCs up to 100 m^3 of active volume have already been successfully operated [25,26], showing the feasibility of very large detectors with large active masses.

2.1. The Optical Readout

Gas luminescence is a well-studied and established mechanism: charged particles traveling in the gas can ionize atoms and molecules but can also excite them. During the de-excitation processes, photons are emitted. The amount and spectrum of light produced strongly depends on the gas, on its density and on the possible presence and strength of an electric field. In most common gas mixtures, the number of emitted photons per avalanche electron can vary between 10^{-2} and 10^{-1} [27–30].

The idea of detecting the light produced during the multiplication processes, proposed many years ago [31], has received renewed attention in recent years. The optical readout approach, in fact, offers several advantages:

- Highly performing optical sensors are being developed for commercial applications and can be easily procured;
- Light sensors can be installed outside the sensitive volume, reducing the interference with high-voltage operation and gas contamination;
- The use of suitable lenses allows the possibility of imaging large O(1) m^2 areas with a single sensor while maintaining an O(100) μm effective pixels transverse size.

In recent years, an increasing number of tracking detectors have started employing micro-pattern gaseous detectors (MPGDs). Their major advantages are their very high achievable granularity and rate capability, together with mechanical robustness. The production technology for MPGDs nowadays guarantees very high-quality devices, providing stable and uniform operation. In particular, GEMs [32] have already been used to equip very large areas with high spacial and time resolution [25], and have more recently been employed coupled to pixelised light sensors, showing very good performances [27,33–35].

Charge coupled devices (CCD) have been widely used in the past as high granularity light sensors for optical TPC approaches [35–37]. CCDs' main limitation for the study of rare events in the 1–100 keV energy range is represented by the high level of readout noise, up to 5 to 10 electrons RMS per pixel. More recently, cameras based on active pixel sensor (APS) technology developed on complementary metal-oxide semiconductors (CMOS) have been developed that can reach tens of millions of pixels with sub-electron readout noise and single photon sensitivity (usually referred as *scientific CMOS* (sCMOS).

The CYGNO collaboration proposed the introduction of sCMOS-based optical devices for GEM readout in 2015 [38]. The high sensitivity of this technique resulted in a very good performance in particle detection not only at the energies of interest for DM searches (as is illustrated in Section 3), but also for minimum ionising particles from both cosmic rays and high energy electrons [34,39–42].

Because the current frame rate available for CCD or sCMOS is still low compared to the temporal extent of typical TPC signals, such devices can provide only 2D projection of the recoil track. In order to achieve 3D track reconstruction, the CYGNO experiment aims at complementing the sCMOS image information with the signal of a fast light sensor (PMT or SiPM) that can provide the track profile along the drift direction.

2.2. The Gas Mixture

The relative photon yield, defined as the ratio between the number of produced photons and the total number of secondary electrons produced in the avalanche process, and in general the overall detector performances, are significantly dependent on the gas characteristics: ionization statistics, transport properties (drift velocity and diffusion), electron multiplication and light production. In the context of optical TPCs for DM searches, CF_4 is a particularly interesting gas because of its well-known property as an efficient scintillator. Furthermore, the large fluorine content provides sensitivity to spin-dependent WIMP-proton interactions. It was demonstrated in previous studies [27] that CF_4-based mixtures have electro-luminescence emission spectra with a large peak around 600 nm, where Si-based sensors (CCD or sCMOS) offer their highest quantum efficiency.

For these reasons, He/CF_4 mixtures in different proportions were extensively studied within the CYGNO project. While the light yield increases for larger amounts of helium, the detector electrical stability improves for higher CF_4 contents. As explained in [43,44], the best compromise was found for a mixture with 60% helium and 40% CF_4. The behaviors of the diffusion coefficients and drift velocity for different electric fields were calculated with Garfield [45,46] and are shown in Figure 1.
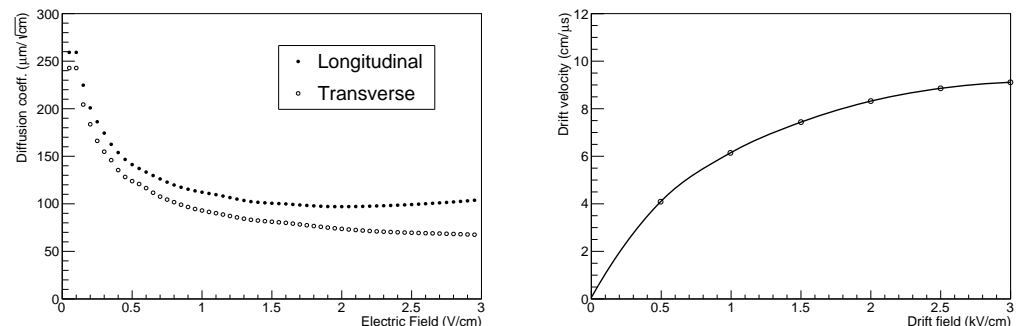
Figure 1. Transverse and longitudinal diffusion coefficients for He/CF_4 60/40 (**left**) and electron drift velocity as a function of the drift field (**right**).

As can be seen from Figure 1, a remarkable additional advantage of the use of CF_4 is the small electron diffusion, which can provide a reduced deterioration of the track's original shape.

For this mixture, an average energy loss per single ionization of 42 eV was estimated. For a minimum ionising particle, 3 ionizations per track millimetre are expected with about 2 electrons per cluster, resulting in an energy loss of about 250 eV/mm. An example of an image of a few cosmic rays is shown in Figure 2: ionization clusters are well-visible along the tracks.
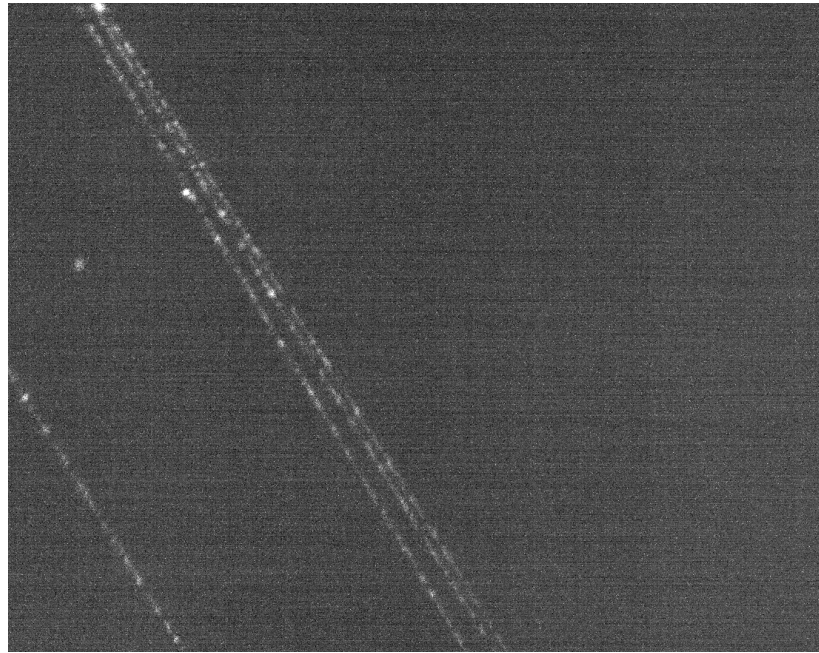
Figure 2. Detail of an image collected with the sCMOS sensor of several tracks in cosmic rays.

The effective ranges of electron and He-nuclei recoils were simulated, respectively, with the GEANT4 [47] and *Stopping and Range of Ions in Matter* (SRIM) software (Visit the http://www.srim.org/ site for more information, accessed on 18 November 2021). The average 3D ranges (i.e., the distance between the production and absorption point) as a function of the particle kinetic energy are shown in Figure 3:

- He-nuclei recoils have a sub-millimetre range up to energies of 100 keV and are thus expected to produce bright spots with sizes mainly dominated by diffusion effects;
- Low-energy (less than 10 keV) electron recoils are, in general, larger then He-nuclei recoils with the same energy and are expected to produce less intense spot-like signals. For a kinetic energy of 10 keV, the electron range becomes longer than 1 mm, and for a few tens of keV, tracks of a few centimetres are expected.
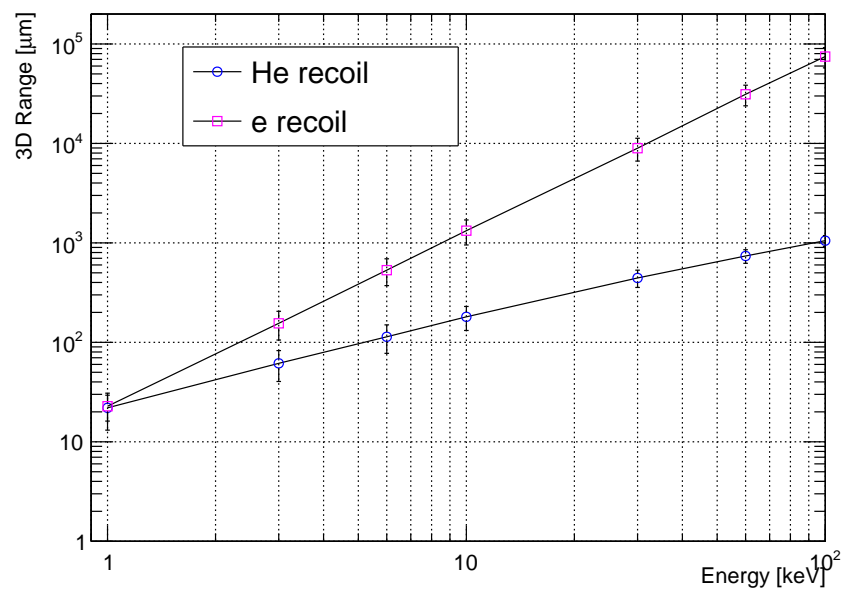
Figure 3. Average 3D distance between the production and absorption point for electron- and He-nucleus recoils as a function of their kinetic energy in a He/CF$_4$ (60/40) gas mixture.

Measurements with other mixtures are also being carried out, including, in particular, the possible use of small amount of hydrocarbons (e.g., C_4H_{10} or CH_4) to add protons as low mass targets. Additionally, alternative gases with reduced global warming power gases (e.g., HFO) are being tested.

3. Experimental Results with LEMON Prototype

The experimental results obtained with the prototype named the Long Elliptical MOdule (LEMON) represents the most comprehensive example currently available of the performance achievable with the CYGNO approach. The LEMON detector, shown in the schematic of Figure 4, is composed of:

- A gas sensitive volume of 7 litres contained in a 20 cm long cylindrical field cage (FC) with an elliptical base with 24 cm and 20 cm axes [A];
- A 24 × 20 cm^2 stack of 3 GEMs as the amplification stage facing the sCMOS camera [D], optically coupled through a 50 cm long (see Equation (2)) black bellow [C] to protect the optics from external light, with the bottom electrode of the last GEM used as the anode;
- A mesh-based semitransparent cathode closing the volume on the opposite side, behind which a PMT [B] is placed.

A more detailed description of this prototype can be found in Ref. [42,48].
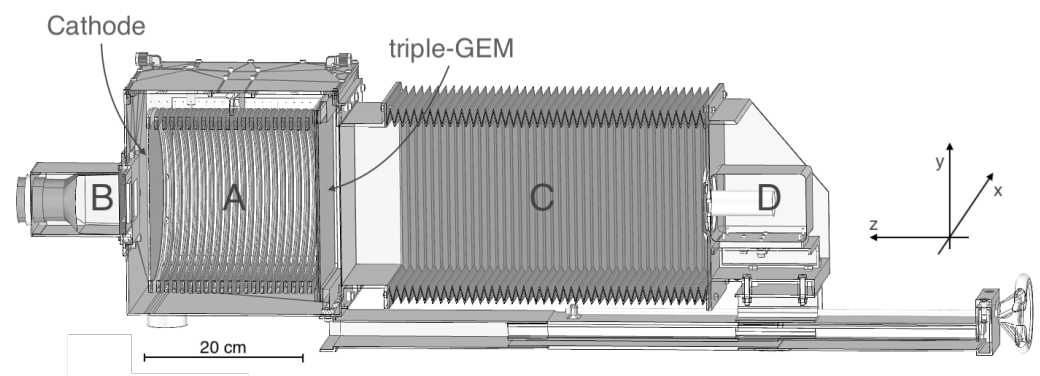
Figure 4. The LEMON prototype [49]. The elliptical sensitive volume (**A**), the fast photo-multiplier (**B**), the optical bellow (**C**) and the sCMOS-based camera (**D**) are indicated.

LEMON standard operating conditions were based on the following sets:

- An He/CF_4 (60/40) gas mixture flux of 200 cc/min;
- An electric drift field within the sensitive volume E_D = 0.5 kV/cm;
- An electric transfer field in the 2 mm gaps between the GEMs E_{Transf} = 2.5 kV/cm;
- A voltage difference across the two sides of each GEM V_{GEM} = 460 V;

According to results presented in [44], in this configuration, an electron multiplication of about 1.5×10^6 is expected.

As anticipated in Section 2.1, high-quality cameras are a crucial ingredient for the experiment results. As a result, an ORCA Flash 4.0 camera (for more details visit www.hamamatsu.com accessed on 18 November 2021) was selected to equip LEMON. This device is based on a 1.33 × 1.33 cm^2 sCMOS sensor, subdivided in 2048 × 2048 pixels with an active area of 6.5 × 6.5 μm^2 each, with a quantum efficiency of 70% at 600 nm and a readout noise of 1.4 electrons RMS. The response and noise level of this sensor were tested with a calibrated light source [34]. A response of 0.9 counts/photon was measured together with a RMS fluctuation of the pedestal of 1.3 photons/pixel.

In order to image the large GEM surface, the camera is equipped with a Schneider lens with a 25.6 mm focal length f and a 0.95 aperture a. Since at a distance d the lens provides a de-magnification of

$$\delta = \frac{f}{d-f} \tag{2}$$

the camera optical system is placed at d = 52.6 cm distance from the GEMs in order to image a 26×26 cm^2 area. The solid angle covered by the sensor, which in turn determines the geometrical acceptance of photons, is given by

$$\Omega = \frac{1}{(4(1/\delta + 1) \times a)^2}$$

resulting in 1.6×10^{-4} for the LEMON layout.

In order to complement the 2D track projection recorded by the sCMOS with the track trajectory along the drift direction, the arrival time profile of the primary electrons could be extracted from the signal induced on the third GEM bottom electrode. Nonetheless, this is expected (and explicitly shown in [39]) to suffer from considerable noise (typically due to jitter on the high voltage supply line) that could prevent signal detection at the low energies at play. To overcome this limitation, a light track time profile was concurrently readout by a Photonics XP3392 Photo Multiplier Tube (PMT), each with a 5 ns rise-time, a maximum QE of 12% for 420 nm and a 76 mm square-window, providing sensitivity to a single photon and significantly reduced noise with respect to the GEM electric signal.

The performances of LEMON has been tested in recent years at the INFN Laboratori Nazionali di Frascati (LNF) overground laboratory by means of radioactive sources (^{55}Fe, AmBe), high-energy (450 MeV) electrons from a beam at the Beam Test Facility (BTF, [50,51]) and cosmic rays, and are summarised in the following.

3.1. Operation Stability

The performance and long-term stability of LEMON was tested for a month long run, during which the detector was exposed to environmental radioactivity, cosmic rays and a ^{55}Fe source [43]. During the whole period, all currents drawn by the high-voltage channels supplying the electrodes of the GEM stack were monitored and recorded to identify sudden and large increases that could indicate discharges or other electrostatic issues. During the test, two different kinds of electrostatic instabilities were observed:

- Hot-spots appearing on the GEM surface. While in some cases these would fade out with time, sometimes they started to slowly grow up to tens of nA (on a time scale of minutes). These are very likely due to self-sustaining micro-discharges happening in one or a few GEM holes;
- High charge density due to very high ionizing particles or charge accumulation on electrode imperfections can suddenly discharge across GEM holes. In these events, a sudden increase in the drawn current is recorded with a voltage restoring on the electrodes through 10 Ω protection resistors on a time basis of a few seconds. Even if these events are less frequent than hot spots, they can be dangerous for the GEM structure and the energy released in the discharge can, in principle, damage it.

An automatic recovery procedure was implemented, triggered by the raising of the GEM currents, which was able to recover both hot-spots and discharges by lowering and gradually restoring the GEM voltage operating conditions in a few minutes.

An average of 16 such instabilities per day were observed and the total dead time introduced by the recovering procedures was less than 4%. A detailed analysis of the time interval between two consecutive phenomena did not show any correlation between two subsequent events, nor any increase of their rates. This study demonstrated that the detector operation looked very safe and stable, and the obtained performance is considered to be satisfactory. Different gas proportions were tested, and a lower amount of CF$_4$ resulted in a less stable electrostatic configuration.

3.2. Light Yield and Energy Resolution

The light production was evaluated by analysing the response of sCMOS and PMT to interactions in a gas of 5.9 keV X-rays produced by a ^{55}Fe source. The sCMOS images were acquired in a free-running mode (i.e., without using any trigger signal) with an exposure of 100 ms. The sCMOS pixels' pedestal noise was extracted from an average of 100 images acquired in the absence of any light signal and subtracted from each image before the analysis. An elementary clustering algorithm based on the nearest neighbor-cluster (NNC) is applied to 4 × 4 rebinned images to select ^{55}Fe induced energy deposits.

Figure 5 shows, on the left, the light spectrum of the ^{55}Fe events reconstructed from the sCMOS images, and on the right, the integral of the charge signal measured by the PMT.

The average light yields were evaluated from a Polya fit [52] to the two distributions, resulting in an average of 514 ± 63 photons per keV detected by the sCMOS camera (in agreement with results obtained with lower V_{GEM} and E_{Transf} [48]), with an RMS energy resolution of 12% and an average of (12.0 ± 0.2) pC per keV together with an RMS energy resolution of 16% by the PMT charge signal.

The energy resolutions are mainly due to the Poisson's fluctuations of the numbers of primary electrons (8%) and of the gain of the first GEM. The latter term can be simply evaluated to be about 10% by supposing an exponential distribution for it [53], with an average value of 100.
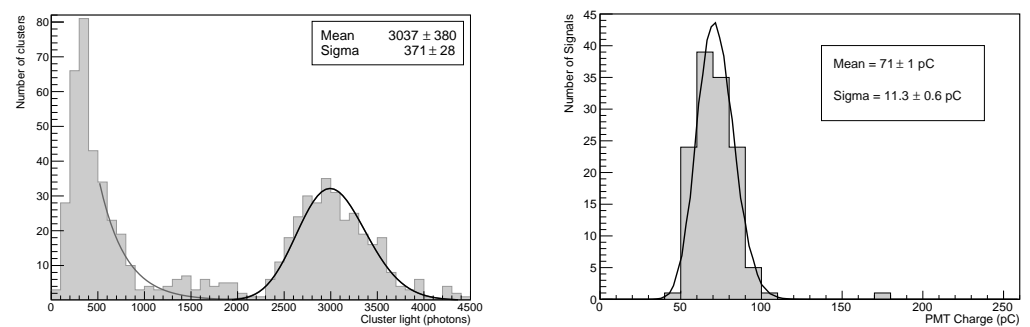
Figure 5. Distribution of the light content of the ^{55}Fe events reconstructed from the sCMOS images (**left**), and distribution of the charge measured by the PMT signals (**right**).

3.3. Detection Efficiency

The detection efficiency along the whole 7 litre sensitive volume was studied acquiring sCMOS images by changing the electric field strength within the field cage (drift field) and the position of a collimated ^{55}Fe source in order to vary the X-ray interaction distance to the amplification region. Figure 6 shows, on the left, the number of reconstructed ^{55}Fe spots in the sCMOS images with the algorithm illustrated in Section 3.2 as a function of drift field (E_D), normalized to the value obtained for E_D = 600 V/cm. For E_D larger than 300 V/cm, a plateau is found, suggesting a full detection efficiency. The right panel of Figure 6 shows the dependence of the number of reconstructed spots normalised to its average value on the source distance from the GEM amplification plane, as measured with an E_D of 600 V/cm. A constant behavior is found in all tested positions, indicating a stable detection efficiency that is not dependent on the interaction point distance from the GEM.
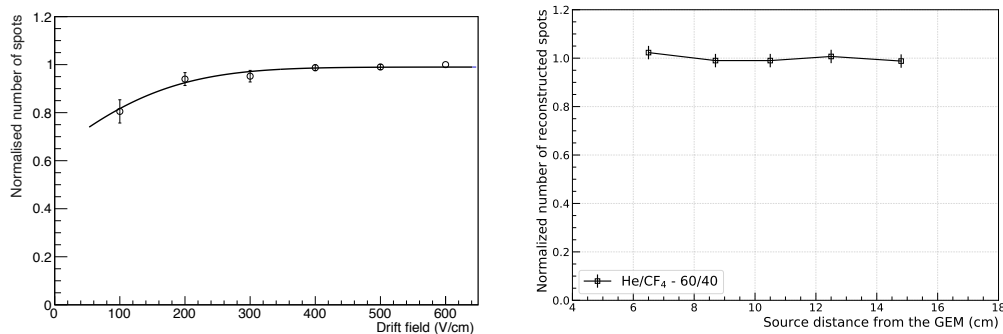
Figure 6. Behavior of the normalized number of ^{55}Fe spots as a function of the drift electric field (**left**) and event depth in the sensitive volume (**right**).

3.4. Track Absolute Distance along the Drift Direction

The possibility to determine the absolute z position of the energy deposit exploiting the electron drift was studied with 450 MeV electrons from the LNF-BTF facility [42]. The transverse diffusion in the drift gap can, in fact, be used to extract the drift length and thus infer the absolute z distance at which the track occurred. Seven millimetre-long track segments were used to evaluate the detector performance for small energy releases.

As described in [49], the light profile transverse to the track direction possesses a Gaussian shape with the total light L being proportional to $\sigma \times$ A (where σ is the RMS and A is the amplitude of the Gaussian). Because of the attachment effect in gas [54], the probability for an electron to reach the GEM stack decreases exponentially with a mean free path λ (and thus $L = L_0 e^{-z/\lambda}$). Since σ is expected to increase as $\sqrt{z}$ because of diffusion in gas, the ratio η, defined as $\sigma/$A, is expected, at a first order approximation, to grow quadratically with the drift distance [42].

Similarly, longitudinal electron diffusion modifies the electron time of arrival on the GEM and thus the time structure of the signal recorded by the PMT. Additionally, in this case, the ratio $\eta_{PMT} = \sigma_{PMT}/A_{PMT}$ is expected to increase with z.

Figure 7 shows the dependence of η and η_{PMT} as a function of z with a superimposed quadratic fit.
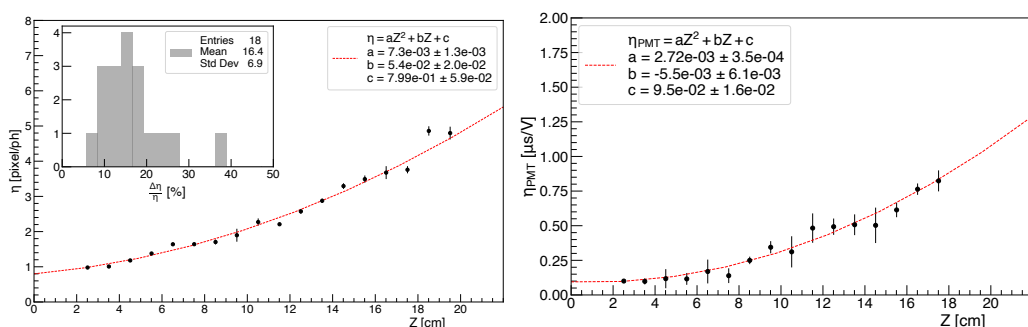
Figure 7. Dependence of η on the left and η_{PMT} on the right as a function of the track distance from the GEM (see text for details).

The inset shows the distribution of the ratio between the RMS and the average values of the spectra of η obtained at the various z. These observables can be, therefore, used to evaluate the absolute z with about 15% uncertainty over a 20 cm length [42]. These features will allow the fiducial signal volume to be selected, therefore rejecting background signals coming from the radioactivity of TPC materials, like the cathode or GEMs.

### 3.5. Detection and Identification of Nuclear and Electron Recoils

Thanks to the detailed information provided by the high granularity optical sensor, track properties like the shape, the length and width, and light density, among others, can efficiently be exploited to identify and separate ER which are surely due to background sources from NR which are possible candidates of DM signals.

To quantify these features within the CYGNO experimental approach, a track reconstruction and identification algorithm was developed for the analysis of the sCMOS images called iDBSCAN [55] and based on an adapted version of the well-known Density-Based Spatial Clustering of Applications with Noise (DBSCAN) [56]. The reconstructed clusters were used as seeds for a superclustering algorithm based on Geodesic Active Contours (GAC [57,58]), which gathers together sub-clusters of the energy deposits belonging to a single track. The GAC, exploiting the number of photons in each pixel as a third dimension to the phase space of the points considered, separately identifies clusters displaying different intensity (i.e., energy deposition patterns) which are, therefore, likely belonging to different classes of particles interactions.

The performance of the algorithm was studied using 5.9 keV energy deposits from ^{55}Fe and NR produced by an AmBe source [59]. The 59 keV photons produced by AmBe were nearly completely shielded by a lead shield built around the detector. Data were taken overground at LNF and were, therefore, highly contaminated by cosmic ray particle interactions.

In order to select a pure sample of nuclear recoil candidates produced by the interaction of the neutrons originating from the source and to identify various sources of backgrounds, several cluster shape observables were exploited. Among these, the *slimness* (ξ) was used to mainly distinguish cosmic rays and the light *density* (δ) to discriminate electron from nuclear recoils. The slimness is defined as the ratio of the Gaussian width of the track in the transverse direction over the projected path length. The density is the ratio of the total number of photons detected by all the pixels gathered in the cluster over the total number of pixels.

As shown in Figure 8, by simply exploiting a selection on δ, an ER background rejection in the energy region around 5.9 keV$_{ee}$ of 96.5% (99.2%) was found together with 50% (40%) NR efficiency [59].
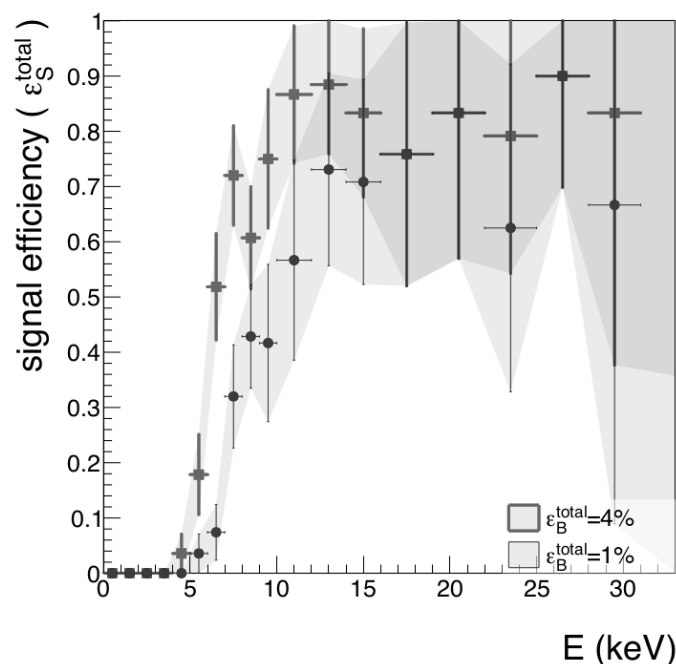
Figure 8. Detection efficiency for nuclear recoils (ϵ_s^{total}) as a function of their detected energy for electron recoils efficiency of 4% (squares) and 1% (circles).

While this cut-based approach is minimalist and could be improved by more sophisticated analyses combining several topological variables as well as the information from PMT waveforms, it shows that a rejection factor larger than 10^2 for electron recoils at $E = 5.9\,\text{keV}$ can be obtained with a gas detector at atmospheric pressure while retaining a high fraction of NR event signals.

4. The CYGNO Experiment Roadmap and Synergies

The CYGNO project will be developed through a staged approach to optimise the apparatus and improve its performance while better mitigating any unexpected cost.

This roadmap, comprises:

- PHASE_0: the installation, in 2022, of a large prototype (50 litres of sensitive volume) underground at the INFN-Laboratori Nazionali del Gran Sasso (LNGS) to study its performance in a low background environment and validate MC simulation;
- PHASE_1: testing, in 2024–2026, of the scalability of the experimental approach on a $O(1)\,\text{m}^3$ detector while studying and minimising the radioactivity background due to apparatus material;
- PHASE_2: depending on the results of the previous phases, a larger scale experiment (30–100 m^3) will be proposed to explore the 1–10 GeV WIMP mass region with high sensitivity for both SI and SD couplings and the possibility of performing the first measurement of low-energy solar neutrinos. In both cases the *directionality capabilities* of the CYGNO approach will allow not only detection of the interactions, but will also provide useful information for astrophysical studies of incoming particles.

The roadmap details and synergies with other projects are outlined in the following sections.

4.1. CYGNO PHASE_0: The LIME Prototype

The Long Imaging ModulE (LIME, shown in Figure 9), is the larger prototype foreseen to conclude the R&D phase of the project. It was conceived to have the same drift length (50 cm) of the final demonstrator (Section 4.2) and the same readout scheme based on triple $33 \times 33\,\text{cm}^2$ thin GEMs (stretched on a plexiglass frame to reduce radioactivity) imaged by a single sCMOS sensor and 4 small PMT symmetrically placed around the sensor at a distance of about 15 cm from it and 25 cm apart from the GEM surface.

The PHASE_1 demonstrator will be based on readout modules having the LIME dimensions and layout. For this reason, its successful assembly and operation will be paramount to substantiate the efforts and confirm the scientific and technological choices towards the 1 m^3 detector.

The new Hamamtsu ORCA-Fusion Camera was employed (https://www.hamamatsu.com/eu/en/product/type/C14440-20UP/index.html, accessed on 18 November 2021) with improved performance with respect to the Orca Flash in terms of reduced noise (0.7 versus 1.4 electrons per pixel), a larger number of pixels (2304×2304 versus 2048×2048) and a larger sensitivity spectrum with a maximum quantum efficiency at 600 nm of 80% versus 70%. The choice of 4 PMT resides in the possibility of better reconstructing the track position and inclination through the center of gravity of the light signal from the 4 sides.

The gas volume is enclosed in a 10 mm thick plexiglass box that provides gas tightness. The field cage is composed by square copper rings, with a rounded shape to avoid discharges, at a 16 mm pitch.

In its underground installation, LIME will be equipped with the same DAQ system and gas system envisaged for the realisation of PHASE_1, which is currently undergoing testing.
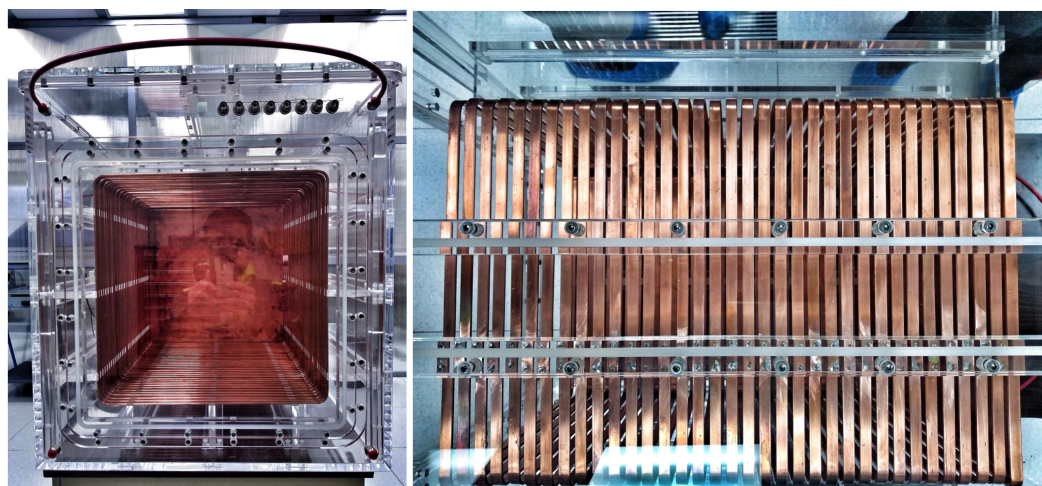
Figure 9. Pictures of the LIME detector. **Left**: front view of the field cage with the copper cathode visible at the end. **Right**: field cage copper rings in the gas vessel.

A response of about 650 ph/keV was measured that has to be compared with 514 ph/keV obtained with LEMON (see Section 3.2) thanks to the larger sensitivity of the Orca Fusion camera. The low sensor noise (about 1 photon/pixel) will allow operation with an effective energy threshold of hundreds of eV. The energy resolution on the ^{55}Fe peak is measured to be 14% across the whole 50 cm drift length, with full efficiency in the full 50 litres volume. Furthermore, LIME has already been operated for one entire month, with its currents continuously monitored and logged, showing comparable stability to LEMON (see Section 3.1).

The installation at LNGS, completed with the PHASE_1 auxiliary systems, will allow:

- The detector performance in low radioactivity and a low pile-up configuration to be tested;
- The real radioactive background present in the site to be characterized, and then the GEANT4 simulation to be validated.

4.2. CYGNO PHASE_1: The O(1) m^3 Demonstrator

Having optimised and assessed all technological aspects with LIME underground tests, the project will move to PHASE_1, with the aim of studying and minimising material radioactivity effects on a real experiment scale, therefore evaluating its sensitivities.

The exact PHASE_1 detector size will depend on the available underground site, which is still under discussion; regardless, a 1 m^3 active volume will be discussed in this paper, schematically shown in Figure 10, with the consideration that the foreseen layout and auxiliary system can be directly and easily adapted to the definitive detector dimensions.

The active volume of the detector will be contained in a gas volume vessel (GVES) realized with PMMA to lower the material intrinsic radioactivity, reduce the gas contamination, and ensure the electrical isolation from the cathode and field cage. The GVES will contain 2 field cages, 500 mm long, with 2 back-to-back TPCs separated by a central aluminised mylar cathode following the DRIFT example [60–62]. This foil is expected to minimise backgrounds induced from recoils by the decay chain of radon.

Each of the 2 end-caps will have an active area of 1 m^2 surface, readout by a matrix of 3×3 modules of 33×33 cm^2 area. Furthermore, each one will be equipped with a stack of 3 GEMS, 1 sCMOS and 4 PMT, identical to the LIME prototype (see Section 4.1).

The GEMs will be assembled adapting the technique discussed in [63]. The mechanical rigidity will be provided by the outer frame that will be anchored to the GVES. The assembled GEM stack will be inserted into the GVES through vertical slits, which will allow an easy substitution of a single GEM foil in case of damage.
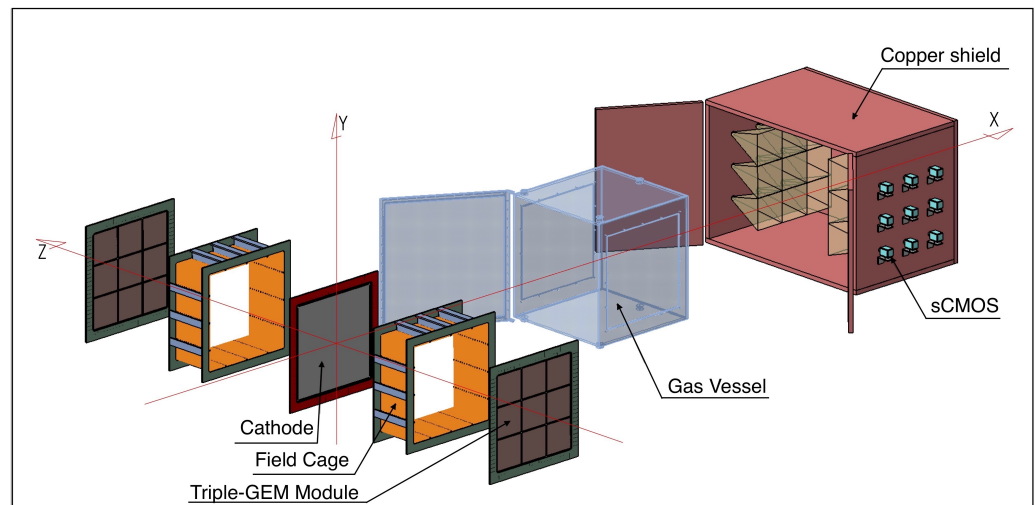
Figure 10. CYGNO PHASE_1 Detector Layout.

The high-voltage system has been conceived with the assumption of independent lines for each electrode of the GEM foils in order to ensure the safe and reliable operation of the detector modules.

The DAQ system will be able to collect synchronized data from cameras and photodetectors and to handle the following specifications:

- Camera exposure from 0.2 to 1 second (1 to 5 Hz frame rate);
- 10 MB of data per picture (5 MP, 16 bits/pixel);
- 12-bit digitization of photodetector waveforms at $\sim$250 MS/s in $\lesssim 1$ μs windows.

Fast responses provided by the PMT will be exploited to trigger the acquisition of sCMOS sensors. Different possible trigger scheme are under evaluation along with the possibility of running either in trigger or trigger-less mode.

The acquisition will be distributed through a redundant system of machines to ensure the system stability. To acquire fast photodetectors, digitization boards are considered. In this scenario, the bottleneck for the acquisition would be the throughput to the disk, typically limited to O(200 MB/s), and some preselection of the images by a farm of CPUs would be needed.

PHASE_1 Shielding Scheme and Material Budget

A GEANT4 based Monte Carlo simulation of the whole apparatus, shown in Figure 10, has been developed to study detector backgrounds and to optimise the choice of shielding and materials.

The effect of the diffused environmental gamma rays and neutron flux was studied. Different configurations of external passive shielding with layers of copper, lead and water were studied with the goal of having less than 10^4 photons/year interacting in the target gas between 1 keV and 20 keV. The choice of this benchmark is backed up by indication from measurements [64,65] and simulations within the CYGNUS collaboration [21] showing that a TPC with 3D readout can reach a 10^5 gamma/year rejection factor at O(keV).

While the use of lead can significantly reduce the overall setup dimensions, the simulation showed that this configuration would require archaeological lead in order not to induce additional background from the shielding, therefore largely raising the cost of this layer. A cost-benefit optimisation of the shielding materials and thicknesses was hence developed, identifying 2 m of water + 5 cm of copper as the optimal configuration. This shielding provides an attenuation by a factor of 10^{-7} for external photons and 5×10^{-5} for external neutrons, reducing the number of expected electron recoils in the active volume below 10^3 cpy (with O(1) cpy nuclear recoils) in the range 1–20 keV.

For the evaluation of the backgrounds generated by detector components, the natural photon radioactivity of the parts expected to give the largest contributions was measured

with high-purity Germanium detectors thanks to the support of LNGS Special Techniques Service. Results are reported in Table 1.

Table 1. Measured activity of the internal detector components expected to produce the largest backgrounds in the active volume. The isotopes in parentheses indicate the activity from that particular part of the decay chain. Upper limits are given at the 90% confidence level.

Component	^{238}U (^{234m}Pa)	^{238}U (^{226}Ra)	^{235}U	^{232}Th (^{228}Ra)	^{232}Th (^{228}Th)	^{40}K
Camera body [Bq/pc]	7	1.8	0.4	2.1	2.1	1.9
Camera lens [Bq/pc]	0.9	0.41	0.031	0.08	0.08	11
GEM foil [Bq/m^2]	<0.104	0.004	<0.002	<0.004	<0.002	<0.045
Acrylic [Bq/kg]		0.003		0.005	0.004	0.035

Regarding the GEMs (made of kapton foils, copper clad on each side), the major source of background is found to come from the frames rather than the foils themselves. For this reason, in the LIME prototype of PHASE_0, the triple 33 × 33 cm^2 GEMs were mounted and stretched on low-radioactivity acrylic frames, with the same technique foreseen to be applied to the PHASE_1 detector.

For what concerns the sCMOS optical system, a large ^{40}K contamination was observed in the lens glass. A high-purity synthetic fused silica (Suprasil®) was selected as an alternative material for the fabrication of the lens, for an expected ~10^4 reduction of the contribution from this item. An overall activity of less than 50 mBq/kg was found in recent measurements performed on a sample at LNGS, confirming the very good properties of this material.

sCMOS cameras have not been employed yet in DM searches, and therefore their intrinsic radioactivity has never been studied or optimised in this context. For this reason, an extensive program working in close contact with sCMOS camera producer companies and with LNGS Services to assess this aspect within our experimental approach has started. Gamma spectroscopy of several sCMOS cameras as a whole was performed, including models from companies other than Hamamatsu, and verified that all display similar activities in the O(10) Bq/piece. The measured activities of the Hamamatsu Orca Fusion are shown in Table 1. A camera was disassembled in 20 different pieces, which are currently under measurement in order to pinpoint the components introducing the largest radioactivity contamination and possibly replace them by cleaner options. Given the very large sCMOS activity, in the PHASE_1 design, they are foreseen to be shielded by the 5 cm copper layer on all sides, except for the one facing the GEMs.

Starting from these considerations, a background evaluation for a 1 m^3 PHASE_1 detector was developed that includes the external gamma and neutron flux contribution with the copper and water shielding discussed above and the radioactivity contribution of the main internal components. For the latter, the values measured at LNGS for the GEMs, camera lens, camera body and acrylic for the gas vessel and data from the literature for the Cu of the cathode and the field cage rings [66] were employed. This study showed that O(10^3) nuclear recoils and O(10^6) electron recoils per year are expected in the sensitive volume, with energy in the 0–20 keV range. It must be noticed that the alphas produced by the GEMs represent the largest contribution to the total NR rate and are absorbed in the gas within 5 cm from them. As described in Section 3.4, by exploiting the effect of diffusion in gas, the track absolute distance from the GEM can be evaluated with a resolution better than 20%. Therefore, this NR background is expected to be reduced to zero with a suitable selection on the drift distance without a significant reduction of the detector fiducial volume. Apart from the current lens, the largest amount of electron recoils is produced by the sCMOS cameras, and, at a second order, by the GEMs.

This study represents the current evaluation of the expected backgrounds for a 1 m^3 detector. Therefore it is the starting point for the optimisation and assessment of the background level, which will be further minimised by the detailed study of the GEM, sCMOS and optics materials.

4.3. CYGNO PHASE_2

A CYGNO detector with a volume of the order of several tens of cubic meters would be able to generate a significant contribution to the search and study of DM in the mass region below 10 GeV, both for SI and SD coupling. In case of appearance of signals or evidence of interactions not due to ordinary matter, the information provided by a directional detector (interaction position, incoming particle direction and energy) will be fundamental to positively confirm the galactic origin of the detected signal as DM and determine its properties.

Such a detector could furthermore provide the first directional measurement of solar neutrinos from the pp chain, possibly extending to lower energies the Borexino measurement, as will be illustrated in Section 5.3.

As an example, Figure 11 shows how a 30 m^3 sensitive volume apparatus with all its shields (for a total volume of 2×10^3 m^3) would fit into the LNGS experimental Hall C.
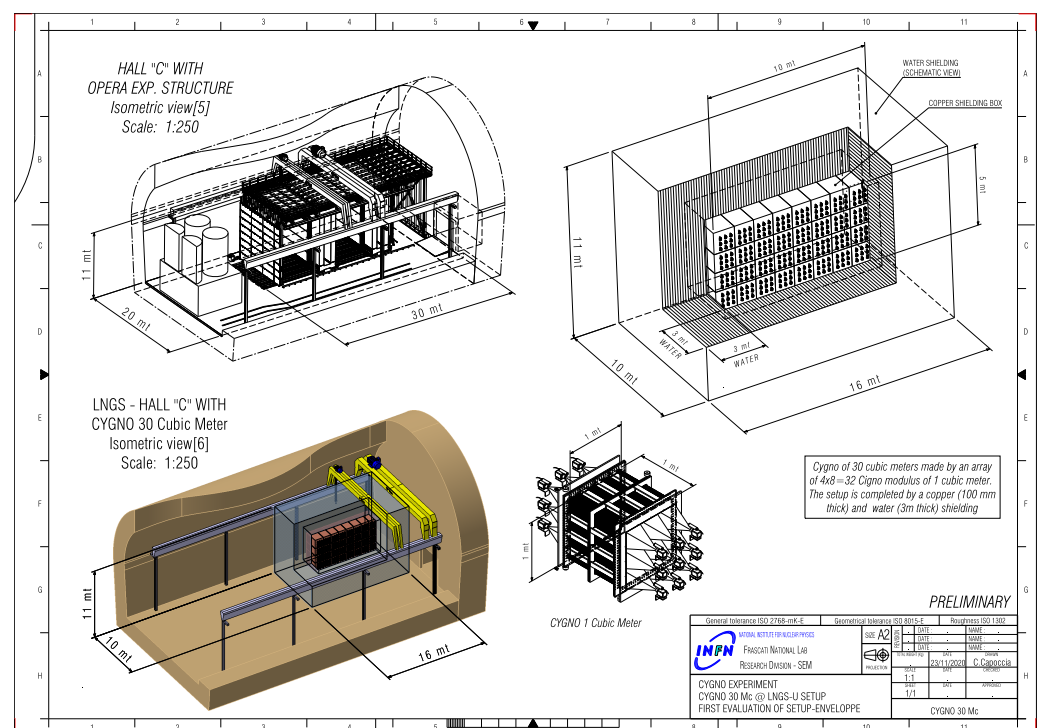

Figure 11. CYGNO PHASE_2 possible setup.

The development of such a detector in terms of intrinsic background minimisation, performance and costs would, of course, require an improved scalable design, materials and readout. The possible improvements include, but are not limited to, the following:

- The development of custom sCMOS sensors, with features focused on CYGNO requirements: low noise, high sensitivity and reduced intrinsic radioactivity together with a lower production cost;
- The design and realisation of low-radioactivity lenses with fixed focus and large aperture;
- The reduction of the intrinsic detector material radioactivity, with the lesson learned after the results obtained with PHASE_1;
- The development of innovative gas mixtures for optical readout (illustrated in the following sub-sections) to boost the tracking performances and improve sensitivity for low energy releases.

4.4. Hydrogen Rich Gas Mixtures

The presence of low-mass nuclei as targets in the gas mixture improves detector performance mostly in the low DM mass region:

- Momentum transfer is more efficient, as shown in Equation (1);
- Longer lengths of light nuclear recoils in gas produces tracks which are more easy to detect and with a clearer direction.

The collaboration is studying the effect of the addition of a small percentage of iC_4H_{10} (1–5%) to the He/CF_4 gas mixture. First results demonstrate that, even if the number of photons collected per keV released decreases up to a factor of 3 (with a 5% addition), light signals are still clear and well-visible. Studies on this and other hydrogen rich mixtures are still going-on and represent a very promising opportunity to lower the effective DM mass threshold.

4.5. INITIUM: an Innovative Negative Ion Time Projection Chamber for Underground Dark Matter Searches

The challenging goal of INITIUM is to develop negative ion drift (NID) operation within the CYGNO optical approach.

Negative ion drift is a peculiar modification of conventional TPCs (NI-TPC) that involves the addition to the gas of a highly electronegative dopant [67,68]. In this configuration, primary electrons produced by an ionizing particle along its track in the gas are captured at very short distances <10–100 μm by electronegative molecules, creating negative ions. These anions drift to the anode, where their additional electron is stripped and gives rise to a standard electron avalanche. Since anions' mobility depends on mass, the difference in the time of arrival of different anions effectively provides a measurement of the position of the event along the drift direction. Full 3D detector fiducialization can be obtained by exploiting this information (as achieved in the DRIFT experiment) and background-free operation over 1 m^3 [61]. Thanks to these two features, NI-TPC readout planes can image a larger volume than conventional TPC approaches, resulting in lower backgrounds and costs per unit mass.

The SF_6 compound has been recently demonstrated to work very well as a negative ion gas between 20 and 100 Torr, including the possibility of high gains and fiducialization via minority charge carriers [69–71]. Compared to the high-vapour pressure, low flash point and low explosive mixture in air of the CS_2 employed by DRIFT, SF_6 has the substantial advantages of much safer handling, combined with easy radon purification and re-circulation, while at the same time increasing the target fluorine mass. The studies proved, for the first time, the feasibility of NID at nearly atmospheric pressure (0.8 atm) with $He/CF_4/SF_6$ at 360/240/10 Torr with triple thin GEMs and charge pixel readout (Timepix) [72].

The goal of INITIUM is to develop a scintillating $He/CF_4/SF_6$-based gas mixture at atmospheric pressure with a low content of SF_6 for NID with optical readout. If NID can be achieved within the optical approach, tracking could be improved by the possibility of reconstructing the track shape along the drift direction by sampling the recorded light at a kHz frame rate. At the moment, such a high rate can be met only by cameras with low resolution and high noise, which are not yet suited for low-energy rare event searches. Nonetheless, given the fast development of the sCMOS technology, progress in short time is possible, which could open the door to this possibility.

5. CYGNO Scientific Goals and Expected Physics Performances

A discussion about the expected sensitivity of CYGNO PHASE 1 to WIMP searches and the tools developed to evaluate it (Section 5.1) is presented in the next sections together with an overview of the experiment potentialities towards additional directional searches.

5.1. WIMP-like DM Searches at Low Masses through Nuclear Recoil Signature

A statistical analysis based on the Bayesian approach to evaluate the sensitivity of the CYGNO PHASE_2 30 m^3 experiment to WIMP searches in the presence of background was performed. Details on the used method are described in the Appendix A.

The CYGNO approach allows the measurement of both the energy and the direction of the track simultaneously, and both of these will be combined to evaluate the number of detected events for the final analysis. Nonetheless, since the angular distribution discriminating power is significantly stronger than the energy spectrum shape, this sensitivity study focuses only on the former for the sake of simplicity. In addition, the background angular distribution can reasonably be assumed to be isotropic in galactic coordinates, while its energy spectrum will highly depend on the exact materials and shielding employed in the experiment; it is therefore difficult to predict with precision at this stage of the project development.

However, the energy threshold plays an important role in the determination of the signal angular distribution together with the target nuclei. Moreover, while the electrons' kinetic energy (eV_{ee}) is very efficiently translated into ionization in gas, an important part of slow NR kinetic energy (eV_{nr}) is loss in scatterings with other nuclei. The fraction of eV_{nr} effectively producing ionization is usually referred to as the quenching factor (QF).

In this sensitivity study, two energy thresholds were assumed: a conservative 1 keV$_{ee}$, backed up by the published results [48], and a realistic value of 0.5 keV$_{ee}$, extrapolated from the improved performances obtained with the PHASE_0 LIME prototype (see Section 4.1). In order to translate this into nuclear recoil energy, a SRIM simulation was developed to evaluate the QFs for the elements in our gas mixture, including hydrogen, given the discussion in Section 4.4. The QFs for H, He, C and F in He/CF$_4$ 60/40 at 1 atm as a function of the nuclear recoil energy E[keV$_{nr}$] were evaluated and found to be in the range 10–30% for keV$_{ee}$ = 100 eV and 60–90% for keV$_{ee}$ = 100 keV. These result in effective energy thresholds of 1.4 (0.8) keV$_r$ for H, 2.1 (1.2) keV$_r$ for He, 3.1 (1.8) keV$_r$ for C and 3.8 (2.2) keV$_r$ for F for a 1 (0.5) keV$_r$ energy deposit.

The signal angular distributions were hence calculated with these effective thresholds in galactic coordinates, starting from [73–75] and neglecting the motion of the Earth, as it was shown to have secondary relevance on the angular distribution. Possible shapes of a DM signal nuclear recoil distribution are shown in 2D galactic coordinates in Figure 12, where the expected anisotropic nature is clearly visible. The final shape of the distribution strongly depends on three elements: the DM mass, the element hit and the energy threshold. With the chosen settings for the analysis, the angular distributions tend to be strongly peaked at low masses and more spread out at heavier masses, where the angular regions strongly suppressed by kinematics are less evident.

In order to establish the credible interval (CI) of the sensitivity limits, experiments are simulated by extracting events according to the expected measured angular distributions discussed so far, adding detector effects. Since CYGNO's approach directional capabilities are still under evaluation, for this study, an angular resolution of 30° in the whole detectable range is assumed, as from literature [76] and from the CYGNUS simulation [21], with full head-tail recognition down to the 1 keV$_{ee}$ energy threshold.

A simple flat distribution of the number of expected signal events between 0 and 1000 is used, given that articulated signal prior probabilities cannot be assumed without risking biases, because the actual cross-section of DM with protons is unknown. Indeed, events per year is a non-negative defined variable, and due to current limits in the DM community, it is hardly believable that more than 1000 events per year would be produced in the CYGNO detector.

The number of expected background events for CYGNO PHASE_2 cannot easily be predicted at this stage of the project, since it will depend on the outcome of PHASE_0 and PHASE_1 and the possible improvements discussed in Sections 4.3–4.5. For this reason, different possible background scenarios are simulated, with 100, 1000 and 10,000 events per year. For these, a Poissonian prior is used. Measurements with PHASE_1 and

simulations informed from these results will, in the future, allow a better estimate of the background yield.

For each scenario, the actual number of events is randomly extracted from this Poissonian distribution and a direction is assigned to each, randomly sampling the background angular distribution. After applying a Gaussian smearing to account for the resolution, a histogram representing the measured event direction in galactic coordinates is filled, with its binning reflecting the angular resolution. In the hypothesis of only background, no events for the WIMP-induced signal recoils are added. In order to avoid suffering from any underfluctuation of the background (as undersampling), 500 data samples are simulated, and the average result is taken as the final value.

The likelihood of the detected events to be the sum of background plus signal (see Appendix A for details) is evaluated on each data sample. From these, the posterior probability at 90%CI of the number of WIMP-induced recoil is computed and averaged to obtain the final result.
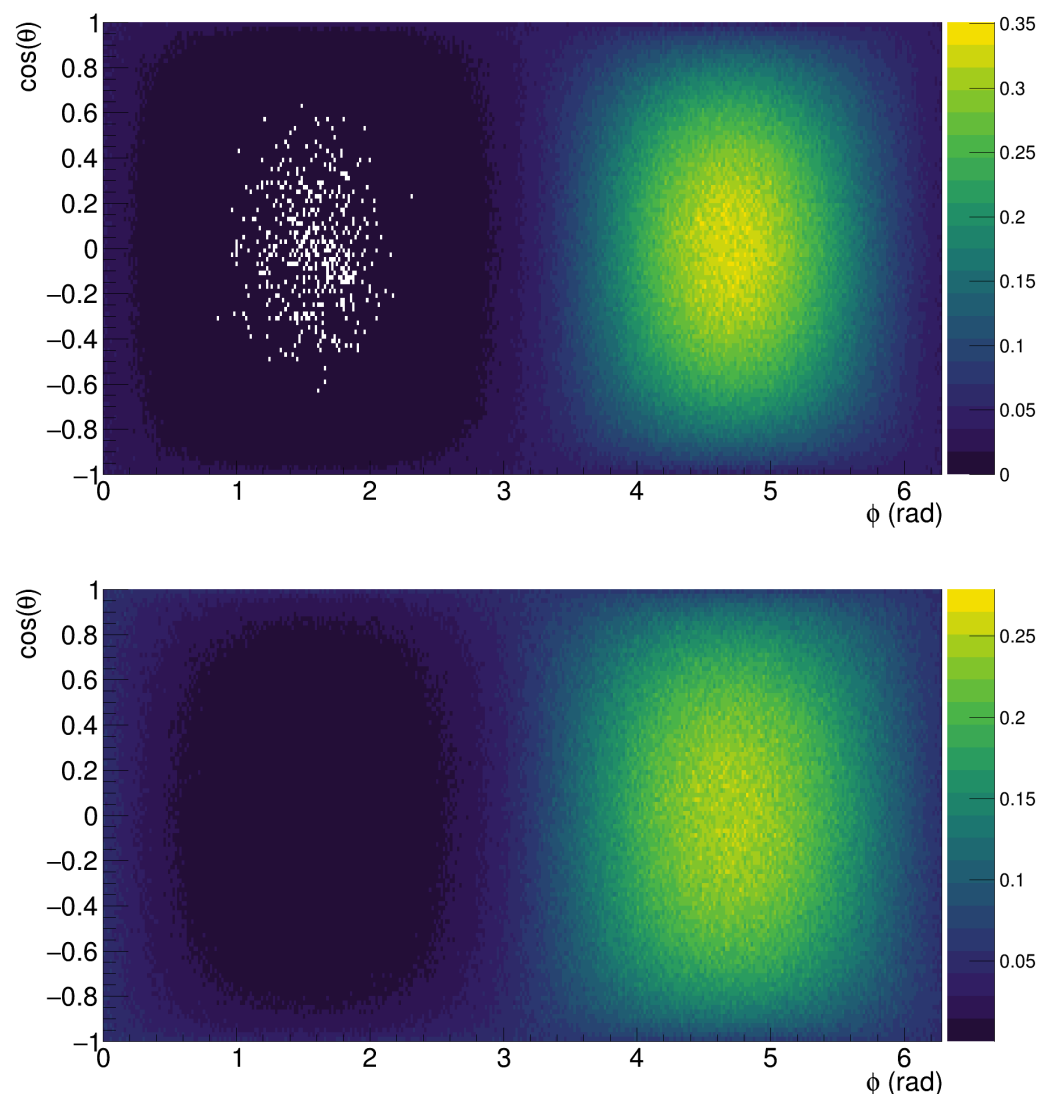
Figure 12. Two examples of the angular distribution of recoils due to DM in Galactic coordinates, obtained by Monte Carlo simulations. Top: helium recoils induced by 10 GeV/c^2 DM. Bottom: fluorine recoils induced by 100 GeV/c^2 DM.

In order to translate this into a limit in the cross-section versus mass parameters space, it is important to take into account that, because the target is a mixture of different elements, both the kinematics of the expected DM-nucleus interactions and the expected

rate calculation influence the probability of each element to be detected differently as a function of the DM mass. This is shown on Figure 13 for a 1 keV$_{ee}$ energy threshold. The region of the DM velocity distribution accessible to detection is limited at lower values by the energy threshold and at higher values by the local escape velocity (here taken as 544 km/s [77]). For low DM masses, the detection of a nuclear recoil is strongly susceptible to the experiment energy threshold. Because of their light masses, hydrogen and helium detection dominate the early part of the figure, and the rising probabilities of carbon and fluorine reflect their different thresholds. At higher DM masses, when the window is quite large, the A^2 cross section enhancement (where A is the atomic number) dominates, making fluorine the most probable detectable element. Figure 13 also displays the minimum detectable DM mass by each element with a 1 (0.5) keV$_{ee}$ energy threshold; that is, 0.5 (0.3) GeV/c^2 for H, 1.0 (0.7) GeV/c^2 for He, 1.9 (1.4) GeV/c^2 for C and 2.5 (1.9) GeV/c^2 for F recoils.
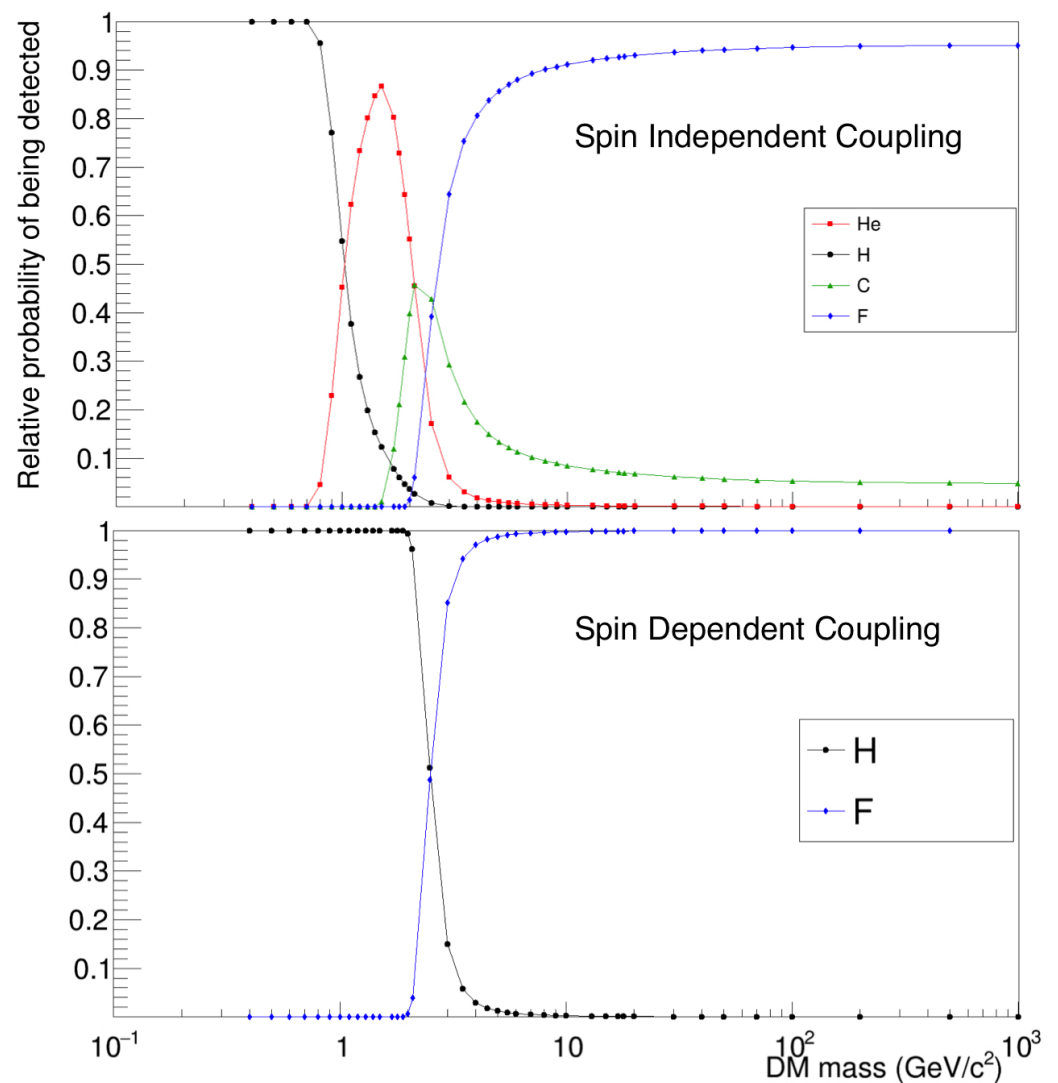
Figure 13. Relative probability of nuclear recoils being detected, given that a recoil was detected, as a function of the DM mass for the SI (**top**) and SD (**bottom**) couplings. An energy threshold of 1 keV$_{ee}$ was used, and the quenching factor corrections are included.

Figure 14 shows in the top part the expected SI limits for a 30 m^3 CYGNO PHASE_2 experiment for a 3-year exposure with different background scenarios and a 1 keV energy threshold. The possible regions explored with an operating threshold of 0.5 keV are shown in the bottom of Figure 14, together with the results that can be reached with a hydrogen-rich gas mixture with 2% isobutane content, as discussed in Section 4.4.
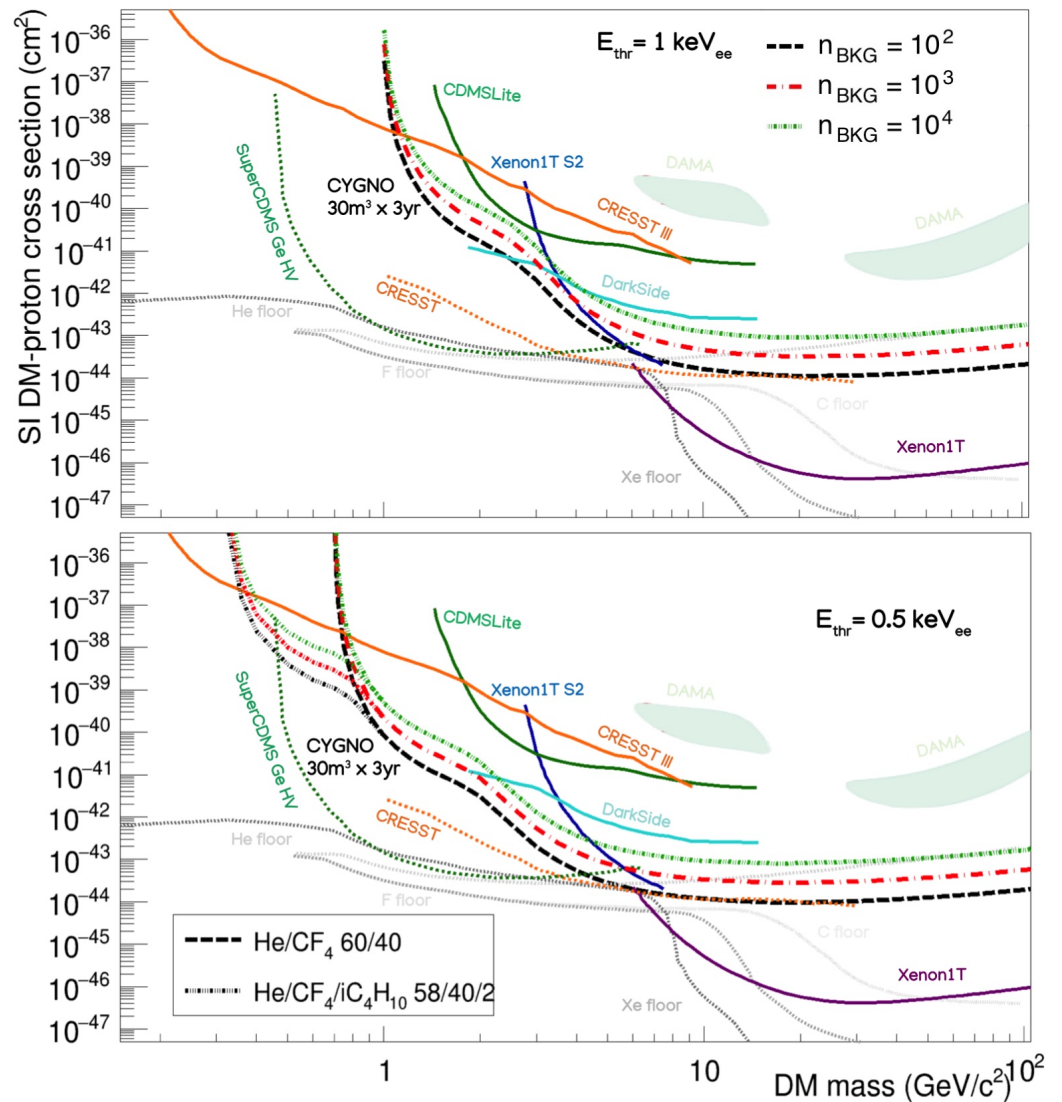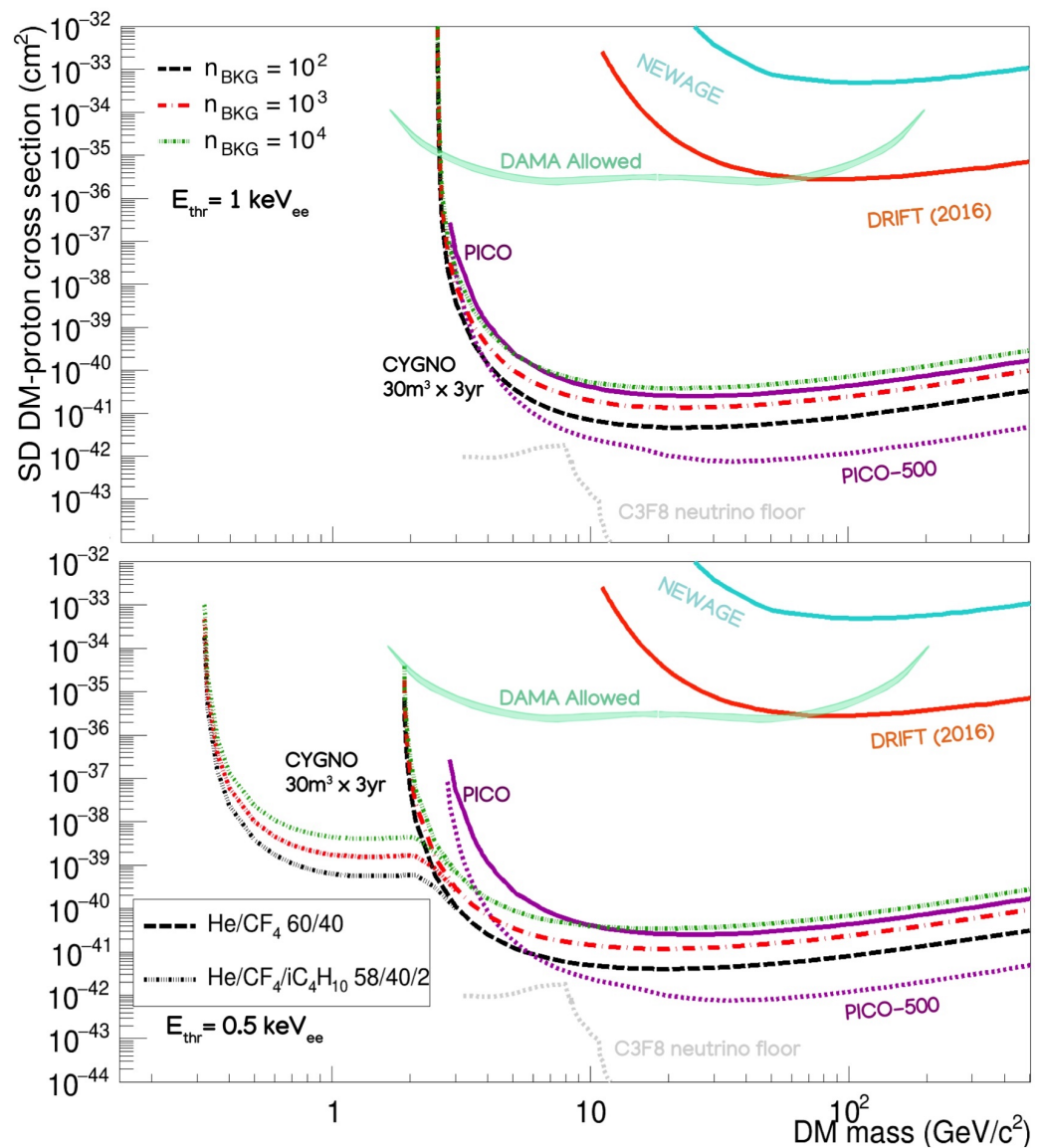

Figure 14. Spin-independent sensitivity for WIMP-nucleon cross-section for 30 m^3 CYGNO detector for 3 years of exposure with different background level assumptions and an operative threshold of 1 keV (top plot) and 0.5 keV (bottom plot). The dashed curves correspond to a HeCF$_4$ 60/40 detector with N$_{bkg}$ = 100 (black), 1000 (red) and 10,000 (dark green). The dotted curves show the sensitivity for a HeCF$_4$:isobutane 58/40/2 mixture. Current bounds from Xenon1T (violet) [78], Xenon1T S2 analysis (blue) [79], DarkSide (cyan) [80], CRESST III (orange) [81] and CDMSLite (green) [82] are also shown. The densely dotted curves show the future expected limits of SuperCDMS Ge (green) [83] and CRESST (orange) [84]. The light gray regions denote DM hints by DAMA [85], while the different gray curves show the neutrino background levels for different targets [86].

The shape of the limit reflects the different nuclear composition of the gas mixture. The lower detectable DM mass obviously corresponds to the one obtainable with the 0.5 keV$_{ee}$ energy threshold and helium quenching factor (hydrogen in the hypothesis of the addition of a small fraction of isobutane). There is a kink on the curve at around 0.9 GeV/c^2 corresponding to the transition from hydrogen-dominated to helium-dominated recoils, and at 3 GeV/c^2, from helium- to fluorine-dominated recoils. The carbon percentage on the total gas mixture (8%) is too low to produce a visible effect on the curve.

Figure 14 shows how all the scenarios considered in this sensitivity evaluation will be able to probe regions in WIMP masses versus cross-section planes not yet explored, therefore significantly contributing to future DM searches for low WIMP masses. While it is true that the expected reach of future SuperCDMS [83], CRESST [84], Darkside low-mass [87] and NEWS-G experiments may be able to cover these regions, all of these will be realised through modes of operation that strongly reduce (if not even completely give up) tools for background discrimination. Each of these approaches implies, therefore, very strict (and not yet demonstrated) requirements on the detector materials' radio-purity and the capability to strongly rely on a precise estimate of the expected backgrounds. As a consequence, any observed signal in this region by these experiments will be difficult to interpret unambiguously as a DM signal. CYGNO's potential of establishing the galactic origin of the detected signal through directional correlation with the Cygnus constellation would therefore constitute a compelling and decisive test to experiment claim in this region, being the only existing approach able to provide a positive identification of a DM signal. CYGNO PHASE_2 realisation would moreover establish the grounds for the development of a multi-site network of modules for a ton-scale CYGNUS project that, through directionality, could perform a precise study of WIMP properties and DM astronomy.

In addition, thanks to the high flourine content, CYGNO PHASE_2 is expected to also be significantly sensitive to SD couplings and be able to explore regions not yet excluded by the PICO experiment in the low background scenario, as shown on the top in Figure 15. The PICO experiment, which possesses the strongest sensitivity among all the existing and planned experiments exploring SD coupling, is based, however, on an energy threshold approach. This implies that signal observation does not allow the measurement of the energy of the detected nuclear recoil and could not, therefore, be translated into a constraint in the masses versus coupling parameter space. Hence, also in this context, a confirmation of the galactic origin of the detected signal would be necessary to establish the properties of the detected WIMP. Moreover, the possibility, now under study, of running with a threshold of 0.5 keV and adding a small amount (2%) of isobutane to the gas mixture would allow DM masses even lower than what is expected for the upgrade of PICO to be reached.

The estimated sensitivities presented in Figures 14 and 15 demonstrate how CYGNO PHASE_2 realisation would therefore constitute a very important and compelling step towards the observation and study of a DM signal in the low WIMP mass region for both SI and SD couplings.

Figure 15. Spin-dependent sensitivity for WIMP–proton cross sections for 30 m^3 CYGNO detector for 3 years of exposure with different background level assumptions and an operative threshold of 1 keV (**top** plot) and 0.5 keV (**bottom** plot). The dashed curves correspond to N_{bkg} = 100 (black), 1000 (red) and 10,000 (dark green). The dotted curves show the sensitivity for a HeCF$_4$:isobutane 58/40/2 mixture. Current bounds from PICO (purple) [88], DRIFT (orange) [61], and NEWAGE (cyan) [89] are also shown. The allowed region by DAMA is denoted by the light green band [90]. The light gray dotted line representing the neutrino floor for C$_3$F$_8$ is also taken from PICO [88].

5.2. Directional Searches for MeV Dark Matter Produced by Supernovae through Nuclear Recoil

While WIMPs still remain highly motivated DM candidates, they are not the only paradigm that can explain the DM presence. Core-collapse supernovae (SN) can reach core temperatures in excess of 30 MeV for O(10) seconds, allowing them to produce vast thermal fluxes of particles with masses O(100) MeV at relativistic speeds [91]. This makes them an ideal astrophysical source for sub-GeV dark matter. The DM candidates emerging from this scenario considered in [91] are dark fermions, but this is not the only possible realisation of such a mechanism. Those particles end up diffusively trapped near the proto-neutron star that forms from the SN core. The dark fermions that do eventually escape are produced with a velocity distribution approximately Maxwell–Boltzmann with semirelativistic velocities ($v \sim 1$, to be compared to classical WIMPs with $v \sim 10^{-3}$),

exhibiting a roughly order-one spread in velocities. This will result in a time-spreading effect during their propagation to Earth of up to 10^5 years for an average galactic SN, creating an overlap in time of various SN. Given the high SN concentration in the galactic center, the emission of > 100 SN is expected to be overlapping in a diffuse flux at Earth at any given time. This resembles the diffuse flux of SN neutrinos comprising the neutrino floor at energies larger than 10 GeV WIMP masses.

Thanks to the large dark fermion momentum, such particles, even of masses of O(10 MeV), would cause, in a detector on Earth, a measurable nuclear recoil of O(keV) to be very hard to distinguish from the one induced by a classic WIMP of the galactic halo by an experiment measuring only the energy deposited in the active volume. Nonetheless, the expected diffuse flux will be strongly peaked towards the galactic center due to the large presence of SN in this region compared to extragalactic sources. Thanks to this high degree of anisotropy, a directional detector is a crucial tool to discriminate MeV SN-produced DM with respect to classical WIMP scenarios. It has in fact recently been shown that a directional approach with realistic experimental performances could distinguish the two scenarios with few detected signal events, while a non-directional detector typically needs a one to two times order of magnitude more signal yield [18]. While this study was performed under the assumption of the absence of background in the detected events, a full estimation of CYGNO sensitivity to this DM candidate scenario with the tools discussed developed for the WIMP physics case in Section 5.1 is under development.

### 5.3. Solar Neutrino Detection through Both Nuclear and Electron Recoil Signature

Solar neutrinos are a well-known background to DM searches. They can interact in the active volume of the detector either via elastic scattering on the electrons (producing an electron recoil) or coherent scattering on the nuclei (producing a nuclear recoil).

Since most current DM experiments possess ER/NR discrimination, typically only the coherent scattering on nuclei is viewed as an irreducible source background, determining the so-called "neutrino floor". Directionality has been extensively recognised as the preeminent tool to identify and discriminate NR induced by solar neutrinos from WIMP signal events [2,21,92]. While a ton-scale experiment is needed to start detecting these events [21], due to the low cross-section, new physics in the neutrino sector (described in terms of new mediators between neutrinos and electrons and/or quarks or in terms of non-standard effective interactions) can increase the rate at low energies [86,93]. This is particularly true for DM masses below 10 GeV, if a new scalar mediator is assumed, where the neutrino floor can be raised by several orders of magnitude, making this accessible to CYGNO PHASE_2.

Concerning ER induced by neutrino-electron elastic scattering, classical DM experiments measuring only the deposited energy in the detector have no means to discriminate them from ER caused by other sources, and hence treat them as background. A detector exhibiting directional capabilities like CYGNO can actually transform these events into a signal. From the ER direction and the Sun position, the angle between the incoming neutrino and the scattered electron can in fact be inferred, providing an unambiguous signal identification just like with the one in directional WIMP searches. Ton-scale gaseous TPC have already been proposed in the past [19,20] to perform solar neutrino spectroscopy. CYGNO's CF_4-based gas mixture appears very attractive in this sense [20] because it possesses a significative electron density (1.05×10^{21} cm^{-3}) with a low Z nuclei, a feature that maximises the number of targets while minimising multiple scattering.

About 1 event/m^3 per year is expected at atmospheric pressure for an ER energy threshold of 20 keV coming from the *pp* chain, making this an extremely interesting physics case for the CYGNO PHASE_2 experiment. Due to the larger multiple scattering suffered by low-energy electrons with respect to nuclei, ER direction determination is more complex than with NR tracks. First results from a dedicated algorithm developed within the collaboration, inspired from X-ray polarimetry [94], shows that 30° 2D angular resolution with sense recognition larger than 80% from the sCMOS images analysis can be achieved at 20 keV in a 1 m^3 detector, improving at higher energies. Figure 16 displays the angular dis-

tribution for ER induced by Solar neutrinos for 20 keV and 100 keV energy thresholds with a 30° × 30° angular resolution. Since background events will be isotropically distributed, this shows how, even with the limited angular resolution assumed, directionality provides an extremely effective means for a high-precision solar neutrino measurement. Moreover, the 20 keV energy threshold assumed for the ER translates to about an 80 keV threshold on the incoming neutrino, opening a new window of opportunity on the *pp* Sun process down to low energy, unreachable to conventional neutrino detectors [19].
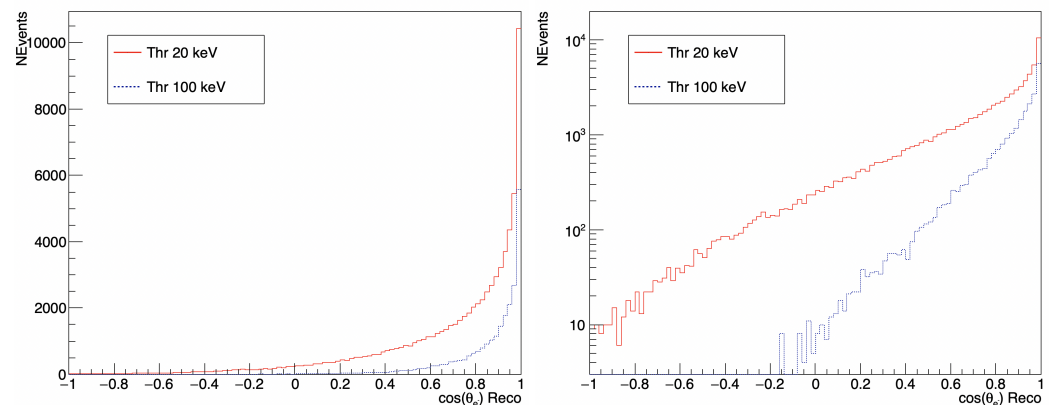
Figure 16. Angular distribution for electron recoils induced by solar neutrinos for 20 keV and 100 keV energy thresholds with a 30° × 30° angular resolution, shown on the right in log scale.

6. Conclusions

In this paper, the case for directional DM searches with gaseous TPC optically read out through the combination of sCMOS images and PMT signals is presented. The performances achieved with a 7-litre prototype based on this approach show the possibility of a $O(keV_{nr})$ detection threshold with 10^2 ER/NR discrimination at 5.9 keV_{ee}. The CYGNO experiment will develop through a staged approach. The underground installation at LNGS of a 50 litre prototype (PHASE_0) is foreseen for the first quarter of 2022, followed by a $O(1)$ m^3 experiment (PHASE_1). PHASE_0 will allow validation of MC simulation and test CYGNO performance in an underground environment. PHASE_1 will be realised to control and minimize the backgrounds from internal materials towards the scalability to larger volume. From the results of these phases, a large-scale experiment (30–100 m^3) will be proposed to explore the 1-10 GeV WIMP mass region with high sensitivity to both SI and SD coupling and directionality. A preliminary sensitivity reach to WIMP searches was hence evaluated for PHASE_2 with different background assumptions, reflecting realistic performance improvements. This study demonstrates that PHASE_2 would bring a significant contribution to WIMP searches, not only by probing parameter spaces unexplored so far, but also being the only approach able to confirm and study any future DM claim by other experiments in this region for both SI and SD couplings. Additional compelling physics cases which are accessible thanks to directional capabilities have also been discussed, for which detailed studies are being carried out.

Appendix A. Statistical Analysis for the Sensitivity Limit Evaluation

The estimation of the expected limits of the CYGNO experiment was performed applying a Bayesian-based method. In principle, this approach allows the probability of any model to be calculated given a certain amount of information (data) related to it. This methodology is rarely used in this field, even though it is recently gaining ground [95–101].

Every model and parameter which is of interest to the specific analysis, as well as experimental data, are all considered connected to a probability distribution and, as such, follow the rules of probability. Exploiting Bayes' theorem, it is possible to find a relation between them and infer a final probability, called posterior, for the desired quantity. In the case of the CYGNO experiment, one is interested in knowing, given a certain number of observed events per year, the probability that some of them are produced by DM-nucleus interactions. Those can be events of background (μ_b) or of signal (μ_s), which are strictly connected to the cross-section of WIMP DM particles with protons. Bayes' theorem can be expressed as follows:

$$p(\mu, \boldsymbol{\theta}|\boldsymbol{D}, H) = \frac{p(\boldsymbol{D}|\mu, \boldsymbol{\theta}, H)\pi(\mu, \boldsymbol{\theta}|H)}{\int_{\Omega}\int_0^{\infty} p(\boldsymbol{D}|\mu, \boldsymbol{\theta}, H)\pi(\mu, \boldsymbol{\theta}|H)d\mu d\boldsymbol{\theta}} \tag{A1}$$

with $p(\boldsymbol{D}|\mu_s, \boldsymbol{\theta}, H)$ representing the likelihood function $L(\mu_s, \boldsymbol{\theta})$.

In Equation (A1), the following notation is used:

- $p(\mu|\boldsymbol{D})$—posterior probability function for the paramenter μ, given $\boldsymbol{D}$;
- $\pi(\mu)$—prior probability of a parameter. This includes the expectations of the parameters as well as constraints and knowledge previously obtained from other experiments;
- μ—free and of interest parameter representing the expected events due to WIMP-induced recoil (μ_s) or background (μ_b), given a certain WIMP mass (the analysis performs a raster scan);
- $\boldsymbol{\theta}$—vector of nuisance parameters, necessary to describe theoretical assumptions and experimental conditions that can affect the results. They can be not completely known and may depend on prior probability distributions. For example, when $\mu = \mu_s$, μ_b, the events expected from the background becomes a nuisance parameter;
- $\boldsymbol{D}$—data set. Can be made of actual experimental data or simulated data;
- H—hypothesis under test. It can be the hypothesis of pure background, H_0, or the one where both background and signal are present, H_1;
- Ω—nuisance parameters space.

The likelihood function used to obtain the results shown in Section 5.1 is defined as:

$$p(\boldsymbol{D}|\mu_s, \mu_b, H_1) = (\mu_b + \mu_s)^{Nevt}e^{-(\mu_b+\mu_s)}\prod_{i=1}^{N_{\text{bins}}}\left[\left(\frac{\mu_b}{\mu_b + \mu_s}P_{i,b} + \frac{\mu_s}{\mu_b + \mu_s}P_{i,s}\right)^{n_i}\frac{1}{n_i!}\right] \tag{A2}$$

with:

- N_{evt}—total number of events of the data sample;
- i—index representing the bin of the histogram in the 2D angular galactic coordinates;
- n_i—number of events occurring in the i-th bin;
- μ—the expected events due to WIMP-induced recoil (μ_s) or background (μ_b), given a certain WIMP mass;
- $P_{i,x}$—the probability of single event to end up in the i-th bin, according to x model (background or signal).

The $P_{i,x}$ marginalized probability includes the effects due to the theoretical angular distribution, the migration from one bin to another caused by resolution effects, and which element recoils. Being in the context of estimating the limits of the CYGNO experiment when data results are consistent with a pure background hypothesis, once the posterior probability of the parameter μ_s is evaluated, it is possible to compute the upper bound as the 90% credible interval (C.I.). This is defined as follows:

$$\mu_s(90\%CI) : \int_0^{\mu_s(90\%CI)} p(\mu_s|\boldsymbol{D}, H_1) d\mu_s = 0.9 \qquad (A3)$$

where $p(\mu_s|\boldsymbol{D}, H_1)$ is the posterior probability marginalised over the nuisance parameters. This value represents the limit under which the true value of μ_s is, with a 90% probability.

References

1. Bertone, G.; Hooper, D.; Silk, J. Particle dark matter: Evidence, candidates and constraints. *Phys. Rept.* **2005**, *405*, 279–390. [CrossRef]
2. Mayet, F.; Green, A.M.; Battat, J.B.R.; Billard, J.; Bozorgnia, N.; Gelmini, G.B.; Gondolo, P.; Kavanagh, B.J.; Lee, S.K.; Loomba, D.; et al. A review of the discovery reach of directional Dark Matter detection. *Phys. Rept.* **2016**, *627*, 1–49.
3. Zurek, K.M. Asymmetric Dark Matter: Theories, Signatures, and Constraints. *Phys. Rept.* **2014**, *537*, 91–121. [CrossRef]
4. Petraki, K.; Volkas, R.R. Review of asymmetric dark matter. *Int. J. Mod. Phys. A* **2013**, *28*, 1330028. [CrossRef]
5. Hochberg, Y.; Kuflik, E.; Murayama, H.; Volansky, T.; Wacker, J.G. Model for Thermal Relic Dark Matter of Strongly Interacting Massive Particles. *Phys. Rev. Lett.* **2015**, *115*, 021301. [CrossRef] [PubMed]
6. Essig, R.; Mardon, J.; Volansky, T. Direct Detection of Sub-GeV Dark Matter. *Phys. Rev. D* **2012**, *85*, 076007. [CrossRef]
7. Essig, R.; Manalaysay, A.; Mardon, J.; Sorensen, P.; Volansky, T. First Direct Detection Limits on sub-GeV Dark Matter from XENON10. *Phys. Rev. Lett.* **2012**, *109*, 021301. [CrossRef]
8. Agnes, P.; Albuquerque, I.F.M.; Alexander, T.; Alton, A.K.; Araujo, G.R.; Asner, D.M.; Ave, M.; Back, H.O.; Baldin, B.; Batignani, G.; et al. Constraints on Sub-GeV Dark-Matter–Electron Scattering from the DarkSide-50 Experiment. *Phys. Rev. Lett.* **2018**, *121*, 111303. [CrossRef] [PubMed]
9. Crisler, M.; Essig, R.; Estrada, J.; Fernandez, G.; Tiffenberg, J.; Sofo haro, M.; Volansky, T.; Yu, T.T. SENSEI: First Direct-Detection Constraints on sub-GeV Dark Matter from a Surface Run. *Phys. Rev. Lett.* **2018**, *121*, 061803. [CrossRef]
10. Agnese, R.; Aralis, T.; Aramaki, T.; Arnquist, I.J.; Azadbakht, E.; Baker, W.; Banik, S.; Barker, D.; Bauer, D.A.; Binder, T.; et al. First Dark Matter Constraints from a SuperCDMS Single-Charge Sensitive Detector. *Phys. Rev. Lett.* **2018**, *121*, 051301; [Erratum: *Phys. Rev. Lett.* **2019**, *122*, 069901]. [CrossRef] [PubMed]
11. Aprile, E.; Aalbers, J.; Agostini, F.; Alfonsi, M.; Althueser, L.; Amaro, F.D.; Antochi, V.C.; Angelino, E.; Angevaare, J.R.; Arneodo, F.; et al. Excess electronic recoil events in XENON1T. *Phys. Rev. D* **2020**, *102*, 072004. [CrossRef]
12. Bernabei, R.; Belli, P.; Montecchia, F.; Nozzoli, F.; Cappella, F.; Incicchitti, A.; Prosperi, D.; Cerulli, R.; Dai, C.J.; He, H.L.; et al. On electromagnetic contributions in WIMP quests. *Int. J. Mod. Phys. A* **2007**, *22*, 3155–3168. [CrossRef]
13. Ibe, M.; Nakano, W.; Shoji, Y.; Suzuki, K. Migdal Effect in Dark Matter Direct Detection Experiments. *J. High Energy Phys.* **2018**, *2018*, 194. [CrossRef]
14. Bell, N.F.; Dent, J.B.; Newstead, J.L.; Sabharwal, S.; Weiler, T.J. Migdal effect and photon bremsstrahlung in effective field theories of dark matter direct detection and coherent elastic neutrino-nucleus scattering. *Phys. Rev. D* **2020**, *101*, 015012. [CrossRef]
15. Dolan, M.J.; Kahlhoefer, F.; McCabe, C. Directly detecting sub-GeV dark matter with electrons from nuclear scattering. *Phys. Rev. Lett.* **2018**, *121*, 101801. [CrossRef] [PubMed]
16. Grilli di Cortona, G.; Messina, A.; Piacentini, S. Migdal effect and photon Bremsstrahlung: Improving the sensitivity to light dark matter of liquid argon experiments. *J. High Energy Phys.* **2020**, *11*, 034. [CrossRef]
17. Cavoto, G.; Luchetta, F.; Polosa, A.D. Sub-GeV Dark Matter Detection with Electron Recoils in Carbon Nanotubes. *Phys. Lett.* **2018**, *B776*, 338–344. [CrossRef]
18. Baracchini, E.; Derocco, W.; Dho, G. Discovering supernova-produced dark matter with directional detectors. *Phys. Rev. D* **2020**, *102*, 075036. [CrossRef]

19. Seguinot, J.; Ypsilantis, T.; Zichichi, A. A High rate solar neutrino detector with energy determination. *Conf. Proc. C* **1992**, *920310*, 289–313.
20. Arpesella, C.; Broggini, C.; Cattadori, C. A possible gas for solar neutrino spectroscopy. *Astropart. Phys.* **1996**, *4*, 333–341. [CrossRef]
21. Vahsen, S.E.; O'Hare, C.A.J.; Lynch, W.A.; Spooner, N.J.C.; Baracchini, E.; Barbeau, P.; Battat, J.B.R.; Crow, B.; Deaconu, C.; Eldridge, C.; et al. CYGNUS: Feasibility of a nuclear recoil observatory with directional sensitivity to dark matter and neutrinos. *arXiv* **2020**, arXiv:2008.12587.
22. Marx, J.N.; Nygren, D.R. The Time Projection Chamber. *Phys. Today* **1978**, *31N10*, 46–53. [CrossRef]
23. Nygren, D.R. The Time Projection Chamber: A New 4 pi Detector for Charged Particles. *eConf* **1974**, *C740805*, 58.
24. Atwood, W.B.; Barczewski, T.; Bauerdickd, L.A.T.; Bellantoni, L.; Blucher, E.; Blum, W.; Boudreau, J.; Boyle, O.; Cinabro, D.; Conway, J.; et al. Performance of the ALEPH time projection chamber. *Nucl. Instrum. Meth. A* **1991**, *306*, 446–458. [CrossRef]
25. Alme, J.; Andres, Y.; Appelshauser, H.; Bablok, S.; Bialas, N.; Bolgen, R.; Bonnes, U.; Bramm, R.; Braun-Munzinger, P.; Campagnolo, R.; et al. The ALICE TPC, a large 3-dimensional tracking device with fast readout for ultra-high multiplicity events. *Nucl. Instrum. Meth. A* **2010**, *622*, 316–367. [CrossRef]
26. Lippmann, C. Upgrade of the ALICE Time Projection Chamber. *Nucl. Instrum. Methods Phys. Res. Sect. Accel. Spectrometers Detect. Assoc. Equip.* **2014**, *958*, 162058.
27. Fraga, M.M.F.R.; Fraga, F.A.F.; Fetal, S.T.G.; Margato, L.M.S.; Ferreira-Marques, R.; Policarpo, A.J.P.L. The GEM scintillation in He CF$_4$, Ar CF$_4$, Ar TEA and Xe TEA mixtures. *Nucl. Instrum. Meth.* **2003**, *A504*, 88–92. [CrossRef]
28. Margato, L.M.S.; Morozov, A.; Fraga, M.M.F.R.; Pereira, L.; Fraga, F.A.F. Effective decay time of CF$_4$ secondary scintillation. *J. Instrum.* **2013**, *8*, P07008. [CrossRef]
29. Baracchini, E.; Benussi, L.; Bianco, S.; Capoccia, C.; Caponero, M.; Cavoto, G.; Cortez, A.; Costa, I.A.; Marco, E.D.; D'Imperio, G.; et al. First evidence of luminescence in a He/CF$_4$ gas mixture induced by non-ionizing electrons. *J. Instrum.* **2020**, *15*, P08018. [CrossRef]
30. Monteiro, C.M.B.; Fernandes, L.M.P.; Veloso, J.F.C.A.; Oliveira, C.A.B.; dos Santos, J.M.F. Secondary scintillation yield from GEM and THGEM gaseous electron multipliers for direct dark matter search. *Phys. Lett. B* **2012**, *714*, 18–23. [CrossRef]
31. Dominik, W.; Zaganidis, N.; Astier, P.; Charpak, G.; Santiard, J.C.; Sauli, F.; Tribollet, E.; Geissbuhler, A.; Townsend, D. A gaseous detector for high accuracy autoradiography of radioactive compounds with optical readout of avalanche positions. *Nucl. Instrum. Meth. A* **1989**, *278*, 779. [CrossRef]
32. Sauli, F. GEM: A new concept for electron amplification in gas detectors. *Nucl. Instrum. Meth. A* **1997**, *386*, 531–534. [CrossRef]
33. Margato, L.M.S.; Fraga, F.A.F.; Fetal, S.T.G.; Fraga, M.M.F.R.; Balau, E.F.S.; Blanco, A.; Ferreira-Marques, R.; Policarpo, A.J.P.L. Performance of an optical readout GEM-based TPC. *Nucl. Instrum. Meth.* **2004**, *A535*, 231–235. [CrossRef]
34. Marafini, M.; Patera, V.; Pinci, D.; Sarti, A.; Sciubba, A.; Spiriti, E. High granularity tracker based on a Triple-GEM optically read by a CMOS-based camera. *J. Instrum.* **2015**, *10*, P12010. [CrossRef]
35. Phan, N.S.; Lee, E.R.; Loomba, D. Imaging ^{55}Fe Electron Tracks in a GEM-based TPC Using a CCD Readout. *arXiv* **2017**, arXiv:1703.09883.
36. Fraga, F.A.F.; Margato, L.M.S.; Fetal, S.T.; Fraga, M.M.F.R.; Ferreira-Marques, R.; Policarpo, A.J.P.L.; Guerard, B.; Oed, A.; Manzini, G.; van Vuure, T. CCD readout of GEM-based neutron detectors. *Nucl. Instrum. Meth. A* **2002**, *478*, 357–361. [CrossRef]
37. Mavrokoridis, K.; Ball, F.; Carroll, J.; Lazos, M.; McCormick, K.J.; Smith, N.A.; Touramanis, C.; Walker, J. Optical Readout of a Two Phase Liquid Argon TPC using CCD Camera and THGEMs. *J. Instrum.* **2014**, *9*, P02006. [CrossRef]
38. Marafini, M.; Patera, V.; Pinci, D.; Sarti, A.; Sciubba, A.; Spiriti, E. ORANGE: A high sensitivity particle tracker based on optically read out GEM. *Nucl. Instrum. Meth.* **2017**, *A845*, 285–288. [CrossRef]
39. Antochi, V.C.; Baracchini, E.; Cavoto, G.; Marco, E.D.; Marafini, M.; Mazzitelli, G.; Pinci, D.; Renga, F.; Tomassini, S.; Voena, C. Combined readout of a triple-GEM detector. *J. Instrum.* **2018**, *13*, P05001. [CrossRef]
40. Marafini, M.; Patera, V.; Pinci, D.; Sarti, A.; Sciubba, A.; Torchia, N.M. Study of the Performance of an Optically Readout Triple-GEM. *IEEE Trans. Nucl. Sci.* **2018**, *65*, 604–608. [CrossRef]
41. Pinci, D.; Baracchini, E.; Cavoto, G.; Marco, E.D.; Marafini, M.; Mazzitelli, G.; Renga, F.; Tomassini, S.; Voena, C. High resolution TPC based on optically readout GEM. *Nucl. Instrum. Methods Phys. Res. Sect. Accel. Spectrometers Detect. Assoc. Equip.* **2018**, *936*, 453–455. [CrossRef]
42. Antochi, V.C.; Cavoto, G.; Costa, I.A.; Marco, E.D.; D'Imperio, G.; Iacoangeli, F.; Marafini, M.; Messina, A.; Pinci, D.; Renga, F.; et al. A GEM-based Optically Readout Time Projection Chamber for charged particle tracking. *arXiv* **2020**, arXiv:physics.ins-det/2005.12272.
43. Baracchini, E., ; Benussi, L.; Bianco, S.; Capoccia, C.; Caponero, M.; Cavoto, G.; Cortez, A.; Costa, I. A.; Di Marco, E.; D'Imperio, G.; et al. Stability and detection performance of a GEM-based Optical Readout TPC with He/CF$_4$ gas mixtures. *J. Instrum.* **2020**, *15*, P10001. [CrossRef]
44. Campagnola, R. Study and Optimization of the Light-Yield of a Triple-GEM Detector. Ph.D. Thesis, Sapienza University of Rome, Roma, Italy, 2018. CERN-THESIS-2018-027.
45. Veenhof, R. Garfield, a drift chamber simulation program. *Conf. Proc. C* **1993**, *9306149*, 66–71.
46. Veenhof, R. GARFIELD, recent developments. *Nucl. Instrum. Meth. A* **1998**, *419*, 726–730. [CrossRef]

47. Agostinelli, S.; Allison, J.; Amako, K.; Apostolakis, J.; Araujo, H.; Arce, P.; Asa, M.; Axen, D.;Banerjee, S.; Barrand, G.; et al. GEANT4: A Simulation toolkit. *Nucl. Instrum. Meth. A* **2003**, *506*, 250–303. [CrossRef]

48. Costa, I.A.; Baracchini, E.; Bellini, F.; Benussi, L.; Bianco, S.; Caponero, M.; Cavoto, G.; D'Imperio, G.; Marco, E.D.; Maccarrone, G.; et al. Performance of optically readout GEM-based TPC with a 55Fe source. *J. Instrum.* **2019**, *14*, P07011. [CrossRef]

49. Antochi, V.; Baracchini, E.; Benussi, L.; Bianco, S.; Capoccia, C.; Caponero, M.; Cavoto, G.; Cortez, A.; Costa, I.; Di Marco, E.; et al. Performance of an optically read out time projection chamber with ultra-relativistic electrons. *Nucl. Instrum. Methods Phys. Res. Sect. A Accel. Spectrometers Detect. Assoc. Equip.* **2021**, *999*, 165209. [CrossRef]

50. Buonomo, B.; Di Giulio, C.; Foggetta, L.G.; Valente, P. A Hardware and Software Overview on the New BTF Transverse Profile Monitor. In Proceedings of the 2016 International Beam Instrumentation Conference, (IBIC'16), Barcelona, Spain, 11–15 September 2016; pp. 818–821. [CrossRef]

51. Valente, P.; Buonomo, B.; Di Giulio, C.; Foggetta, L.G. Frascati Beam-Test Facility (BTF) High Resolution Beam Spot Diagnostics. In Proceedings of the 5th International Beam Instrumentation Conference (IBIC 2016), Barcelona, Spain, 11–15 September 2016; pp. 222–225. [CrossRef]

52. Blum, W.; Rolandi, L.; Riegler, W. *Particle Detection with Drift Chambers*; Particle Acceleration and Detection; Springer: Berlin/Heidelberg, Germany, 2008; ISBN 9783540766834. [CrossRef]

53. Pinci, D. A triple-GEM Detector for the Muon System of the LHCb Experiment. Ph.D. Thesis, Cagliari University, Cagliari, Italy, 2006. Available online: http://cds.cern.ch/record/1005178 (accessed on 18 November 2021).

54. Anderson, W.S.; Armitage, J.C.; Dunn, E.; Heinrich, J.G.; Lu, C.; McDonald, K.T.; Weckel, J.; Zhu, Y. Electron attachment, effective ionization coefficient, and electron drift velocity for CF-4 gas mixtures. *Nucl. Instrum. Meth. A* **1992**, *323*, 273–279. [CrossRef]

55. Baracchini, E.; Benussi, L.; Bianco, S.; Capoccia, C.; Caponero, M.; Cavoto, G.; Cortez, A.; Costa, I. A.; Di Marco, E.; D'Imperio, G.; et al. A density-based clustering algorithm for the CYGNO data analysis. *J. Instrum.* **2020**, *15*, T12003. [CrossRef]

56. Ester, M.; Kriegel, H.P.; Sander, J.; Xu, X. A Density-based Algorithm for Discovering Clusters a Density-based Algorithm for Discovering Clusters in Large Spatial Databases with Noise. In Proceedings of the Second International Conference on Knowledge Discovery and Data Mining (KDD'96), Ortland, OR, USA, 2–4 August 1996; pp. 226–231.

57. Caselles, V.; Kimmel, R.; Sapiro, G. Geodesic Active Contours. *Int. J. Comput. Vis.* **1997**, *22*, 61–79. [CrossRef]

58. Marquez-Neila, P.; Baumela, L.; Alvarez, L. A Morphological Approach to Curvature-Based Evolution of Curves and Surfaces. *IEEE Trans. Pattern Anal. Mach. Intell.* **2014**, *36*, 2–17. [CrossRef] [PubMed]

59. Baracchini, E.; Benussi, L.; Bianco, S.; Capoccia, C.; Caponero, M.; Cavoto, G.; Cortez, A.; Costa, I. A.; Di Marco, E.; D'Imperio, G.; et al. Identification of low energy nuclear recoils in a gas TPC with optical readout. *Meas. Sci. Technol.* **2020**, *32*, 025902. [CrossRef]

60. Daw, E.; Dorofeev, A.; Fox, J.R.; Gauvreau, J.-L.; Ghag, C.; Harmon, L.J.; Harton, J. L.; Gold, M.; Lee, E.R.; Loomba, D.; et al. The DRIFT Directional Dark Matter Experiments. *EAS Publ. Ser.* **2012**, *53*, 11–18. [CrossRef]

61. Battat, J.; Ezeribe, A.; Gauvreau, J.L.; Harton, J.; Lafler, R.; Law, E.; Lee, E.; Loomba, D.; Lumnah, A.; Miller, E.; et al. Low Threshold Results and Limits from the DRIFT Directional Dark Matter Detector. *Astropart. Phys.* **2017**, *91*, 65–74. [CrossRef]

62. Battat, J.B.R.; Daw, E.; Dorofeev, A.; Ezeribe, A.C.; Fox, J.R.; Gauvreau, J.-L.; Gold, M.; Harmon, L.; Harton, J.; Lafler, R.; et al. Reducing DRIFT Backgrounds with a Submicron Aluminized-Mylar Cathode. *Nucl. Instrum. Meth. A* **2015**, *794*, 33–46. [CrossRef]

63. Colaleo, A.; Safonov, A.; Sharma, A.; Tytgat, M. *CMS Technical Design Report for the Muon Endcap GEM Upgrade*; CERN-LHCC-2015-012, CMS-TDR-013; CERN: Geneva, Switzerland, 2015.

64. Riffard, Q.; Santos, D.; Guillaudin, O.; Bosson, G.; Bourrion, O.; Bouvier, J.; Descombes, T.;Muraz, J.-F.; Lebreton, L.; Maire D.; et al. MIMAC low energy electron-recoil discrimination measured with fast neutrons. *J. Instrum.* **2016**, *11*, P08011. [CrossRef]

65. Phan, N.S.; Lauer, R.J.; Lee, E.R.; Loomba, D.; Matthews, J.A.J.; Miller, E.H. GEM-based TPC with CCD Imaging for Directional Dark Matter Detection. *Astropart. Phys.* **2016**, *84*, 82–96. [CrossRef]

66. Castel, J.; Cebrian, S.; Coarasa, I.; Dafni, T.; Galan, J.; Iguaz, F.J.; Irastorza, I.G.; Luzon, G.; Mirallas, H.; Ortiz de Solorzano, A.; et al. Background assessment for the TREX Dark Matter experiment. *Eur. Phys. J. C* **2019**, *79*, 782. [CrossRef]

67. Martoff, C.J.; Snowden-Ifft, D.P.; Ohnuki, T.; Spooner, N.; Lehner, M. Suppressing drift chamber diffusion without magnetic field. *Nucl. Instrum. Meth. A* **2000**, *440*, 355–359. [CrossRef]

68. Ohnuki, T.; Snowden-Ifft, D.P.; Martoff, C.J. Measurement of carbon disulfide anion diffusion in a TPC. *Nucl. Instrum. Meth. A* **2001**, *463*, 142–148. [CrossRef]

69. Phan, N.S.; Lafler, R.; Lauer, R.J.; Lee, E.R.; Loomba, D.; Matthews, J.A.J.; Miller, E.H. The novel properties of SF_6 for directional dark matter experiments. *J. Instrum.* **2017**, *12*, P02012. [CrossRef]

70. Ikeda, T.; Shimada, T.; Ishiura, H.; Nakamura, K.D.; Nakamura, T.; Miuchi, K. Development of a negative ion micro TPC detector with SF_6 gas for the directional dark matter search. *J. Instrum.* **2020**, *15*, P07015. [CrossRef]

71. Lightfoot, P.K.; Spooner, N.J.C.; Lawson, T.B.; Aune, S.; Giomataris, I. First operation of bulk micromegas in low pressure negative ion drift gas mixtures for dark matter searches. *Astropart. Phys.* **2007**, *27*, 490–499. [CrossRef]

72. Baracchini, E.; Cavoto, G.; Mazzitelli, G.; Murtas, F.; Renga, F.; Tomassini, S. Negative Ion Time Projection Chamber operation with SF_6 at nearly atmospheric pressure. *J. Instrum.* **2018**, *13*, P04022. [CrossRef]

73. Lewin, J.; Smith, P. Review of mathematics, numerical factors, and corrections for dark matter experiments based on elastic nuclear recoil. *Astropart. Phys.* **1996**, *6*, 87–112. [CrossRef]

74. Gondolo, P. Recoil momentum spectrum in directional dark matter detectors. *Phys. Rev. D* **2002**, *66*. [CrossRef]

75. Baxter, D.; Bloch, I.M.; Bodnia, E.; Chen, X.; Conrad, J.; Gangi, P.D.; Dobson, J.E.Y.; Durnford, D.; Haselschwardt, S.J.; Kaboth, A.; et al. Recommended conventions for reporting results from direct dark matter searches. *arXiv* **2021**, arXiv:2105.00599.

76. Nakamura, K.; Miuchi, K.; Iwaki, S.; Kubo, H.; Mizumoto, T.; Nishimura, H.; Parker, J.D.;Sawano, T.; Takada, A.; Tanimori, T.; et al. Low pressure gas study for a direction-sensitive dark matter search experiment with MPGD. *J. Instrum.* **2012**, *7*, C02023. [CrossRef]

77. Smith, M.C.; Ruchti, G.R.; Helmi, A.; Wyse, R.F.G.; Fulbright, J.P.; Freeman, K.C.; Navarro, J.F.; Seabroke, G.M.; Steinmetz, M.; Williams, M.; et al. The RAVE survey: Constraining the local Galactic escape speed. *Mon. Not. R. Astron. Soc.* **2007**, *379*, 755–772. [CrossRef]

78. Aprile, E.; Aalbers, J.; Agostini, F.; Alfonsi, M.; Althueser, L.; Amaro, F.; Anthony, M.; Arneodo, F.; Baudis, L.; Bauermeister, B.; et al. Dark Matter Search Results from a One Ton-Year Exposure of XENON1T. *Phys. Rev. Lett.* **2018**, *121*, 111302. [CrossRef] [PubMed]

79. Aprile, E.; Aalbers, J.; Agostini, F.; Alfonsi, M.; Althueser, L.; Amaro, F.; Antochi, V.; Angelino, E.; Arneodo, F.; Barge, D.; et al. Light Dark Matter Search with Ionization Signals in XENON1T. *Phys. Rev. Lett.* **2019**, *123*, 251801. [CrossRef]

80. Agnes, P.; Albuquerque, I.; Alexander, T.; Alton, A.; Araujo, G.; Asner, D.; Ave, M.; Back, H.; Baldin, B.; Batignani, G.; et al. Low-Mass Dark Matter Search with the DarkSide-50 Experiment. *Phys. Rev. Lett.* **2018**, *121*, 081307. [CrossRef] [PubMed]

81. Mancuso, M.; Abdelhameed, A. H.; Angloher, G.; Breier, R.; Bauer, P.; Bento, A.; Bertoldo, E.;Bucci, C.; Canonica, L.; D'Addabbo, A.; et al. Searches for Light Dark Matter with the CRESST-III Experiment. *J. Low Temp. Phys.* **2020**, *199*, 547–555. [CrossRef]

82. Agnese, R.; Anderson, A.; Aralis, T.; Aramaki, T.; Arnquist, I.; Baker, W.; Balakishiyeva, D.; Barker, D.; Basu Thakur, R.; Bauer, D.; et al. Low-mass dark matter search with CDMSlite. *Phys. Rev. D* **2018**, *97*, 022002. [CrossRef]

83. Agnese, R.; Anderson, A.J.; Aramaki, T.; Arnquist, I.; Baker, W.; Barker, D.; Basu Thakur, R.; Bauer, D.A.; Borgland, A.; Bowles, M.A.; et al. Projected Sensitivity of the SuperCDMS SNOLAB experiment. *Phys. Rev. D* **2017**, *95*, 082002. [CrossRef]

84. Willers, M.; Angloher, G.; Bento, A.; Bucci, C.; Canonica, L.; Defay, X.; Erb, A., Feilitzsch, F.v.;Iachellini, N.F.; Gütlein, A.; et al. Direct dark matter search with the CRESST-III experiment - status and perspectives. *J. Phys. Conf. Ser.* **2017**, *888*, 012209. [CrossRef]

85. Savage, C.; Gelmini, G.; Gondolo, P.; Freese, K. Compatibility of DAMA/LIBRA dark matter detection with other searches. *J. Cosmol. Astropart. Phys.* **2009**, *2009*, 010. [CrossRef]

86. Bœhm, C.; Cerdeño, D.G.; Machado, P.A.N.; Olivares-Del Campo, A.; Perdomo, E.; Reid, E. How high is the neutrino floor? *J. Cosmol. Astropart. Phys.* **2019**, *2019*, 043. [CrossRef]

87. Galbiati, C. Future Dark Matter Searches with Low-Radioactivity Argon, by The Global Argon Dark Matter Collaboration. Input to the European Particle Physics Strategy Update. Available online: https://indico.cern.ch/event/765096/contributions/3295671/attachments/1785196/2906164/DarkSide-Argo_ESPP_Dec_17_2017.pdf (accessed on 18 November 2021).

88. Amole, C.; Ardid, M.; Arnquist, I.; Asner, D.; Baxter, D.; Behnke, E.; Bressler, M.; Broerman, B.; Cao, G.; Chen, C.; et al. Dark matter search results from the complete exposure of the PICO-60 C3F8 bubble chamber. *Phys. Rev. D* **2019**, *100*, 022001. [CrossRef]

89. Yakabe, R.; Nakamura, K.; Ikeda, T.; Ito, H.; Yamaguchi, Y.; Taishaku, R.; Nakazawa, M.; Ishiura, H.; Nakamura, T.; Shimada, T.; et al. First limits from a 3d-vector directional dark matter search with the NEWAGE-0.3b' detector. *Prog. Theor. Exp. Phys.* **2020**, *2020*, 113F01. [CrossRef]

90. Savage, C.; Gondolo, P.; Freese, K. Can WIMP spin dependent couplings explain DAMA data, in light of null results from other experiments? *Phys. Rev. D* **2004**, *70*, 123513. [CrossRef]

91. DeRocco, W.; Graham, P.W.; Kasen, D.; Marques-Tavares, G.; Rajendran, S. Supernova signals of light dark matter. *Phys. Rev. D* **2019**, *100*, 075018. [CrossRef]

92. Billard, J.; Strigari, L.; Figueroa-Feliciano, E. Implication of neutrino backgrounds on the reach of next generation dark matter direct detection experiments. *Phys. Rev. D* **2014**, *89*, 023524. [CrossRef]

93. Bertuzzo, E.; Deppisch, F.F.; Kulkarni, S.; Perez Gonzalez, Y.F.; Zukanovich Funchal, R. Dark Matter and Exotic Neutrino Interactions in Direct Detection Searches. *J. High Energy Phys.* **2017**, *2017*, 073. [CrossRef]

94. Soffitta, P.; Muleri, F.; Fabiani, S.; Costa, E.; Bellazzini, R.; Brez, A.; Minuti, M.; Pinchera, M.; Spandre, G. Measurement of the position resolution of the Gas Pixel Detector. *Nucl. Instrum. Meth. A* **2013**, *700*, 99–105. [CrossRef]

95. Roszkowski, L.; Ruiz de Austri, R.; Silk, J.; Trotta, R. On prospects for dark matter indirect detection in the Constrained MSSM. *Phys. Lett. B* **2009**, *671*, 10–14. [CrossRef]

96. Trotta, R.; de Austri, R.R.; Roszkowski, L. Prospects for direct dark matter detection in the constrained MSSM. *New Astron. Rev.* **2007**, *51*, 316–320. doi: 10.1016/j.newar.2006.11.059. [CrossRef]

97. Strege, C.; Trotta, R.; Bertone, G.; Peter, A.H.G.; Scott, P. Fundamental statistical limitations of future dark matter direct detection experiments. *Phys. Rev. D* **2012**, *86*, 023507. [CrossRef]

98. Arina, C. Bayesian analysis of multiple direct detection experiments. *Phys. Dark Universe* **2014**, *5*, 1–17. [CrossRef]

99. Bringmann, T.; Conrad, J.; Cornell, J.M.; Dal, L.A.; Edsjö, J.; Farmer, B.; Kahlhoefer, F.; Kvellestad, A.; Putze, A.; et al. DarkBit: A GAMBIT module for computing dark matter observables and likelihoods. *Eur. Phys. J. C* **2017**, *77*, 831. [CrossRef]

100. Liem, S.; Bertone, G.; Calore, F.; de Austri, R.R.; Tait, T.M.P.; Trotta, R.; Weniger, C. Effective field theory of dark matter: A global analysis. *J. High Energy Phys.* **2016**, *2016*, 77. [CrossRef]

101. Messina, A.; Nardecchia, M.; Piacentini, S. Annual modulations from secular variations: Not relaxing DAMA? *J. Cosmol. Astropart. Phys.* **2020**, *2020*, 037. [CrossRef]